ABSTRACT

Title of Thesis: VARIATIONS OF ENGINE PARTICULATE MATTER IN A MINIATURE DILUTION TUNNEL

Eric M Kommer, Master of Science, 2003

Thesis directed by: Assistant Professor Steven G. Buckley
Department of Mechanical Engineering

Measurement of diesel and spark ignition engine particulate emissions is of wide interest due to current research demonstrating that inhalation of nanoparticles may cause serious health problems. Both experimental and computational methods were used to investigate fluid and particle flows through a miniature dilution tunnel similar to those commonly used to sample particulate emissions from engines to help explain observed varabilities and bias, and to improve the repeatability of results. Laser Doppler Velocimetry, flow visualization, and a commercial CFD code were used to measure the flow field inside the apparatus. Slugs of NOx calibration gas and a high speed NOx concentration meter were used to measure mean velocities through the apparatus. An artificial aerosol generator was used in conjunction with a Scanning Mobility Particle Sizer (SMPS) to determine how tunnel geometry affects particle size distributions. These results were compared to a Monte Carlo type numerical simulation, accounting for Brownian motion and fluctuating turbulent velocities.

A comparison between the flow field measurement techniques, CFD results and published literature show the behavior similar to that expected from an enclosed turbulent jet. Centerline velocities of the jet decay as predicted by the literature with radial velocity profiles matching closely. A comparison between the SMPS results and the predicted size distribution at a particular point downstream from the Monte Carlo model exhibit similar magnitudes but do not follow the same trends, indicating that more refined modeling is needed. Nevertheless, this research strongly indicates that sampled submicron particle size distributions in dilution tunnels will be heavily influenced by the character of the turbulent mixing and the axial and radial locations of the sampling probe.

VARIATIONS OF ENGINE PARTICULATE MATTER IN A MINIATURE DILUTION TUNNEL

by

Eric M Kommer

Thesis submitted to the Faculty of the Graduate School of the
University of Maryland, College Park in partial fulfillment
of the requirements for the degree of
Master of Science
2003

Advisory Committee:

Assistant Professor Steven Buckley, Chair/Advisor
Professor David Holloway
Associate Professor Gregory Jackson

TABLE OF CONTENTS

LIST OF FIGURES

CHAPTER 1 Introduction

1.1 Background

Exhaust emissions from internal combustion engines is of great theoretical and practical interest, both for environmental engineers and also engine manufacturers. The effects of engine emissions are evident to anyone living in an urban environment. Engines across a range of sizes and types from modern spark ignition in an automobile to a heavy diesel on a Navy ship all contribute to emissions that can be harmful to public health. EPA standards regulate emissions of nitrous oxides, carbon monoxide and hydrocarbons, which are important not just from a health standpoint but also for engine efficiency.

In recent years particulate emissions have become increasingly important. Particulate emissions contribute to visible smog and pollution, which is most apparent to the average citizen. Particulates also have harmful health effects, which have only recently been understood. When aerosol particles are inhaled, they may deposit in the airways and lungs, and have the chance to release toxic components into the body. Recent medical studies have shown that smaller sized particles may in fact be more dangerous that larger ones that the body can more easily eliminate.[2] These submicron "nanoparticles," once thought to be so small as to simply pass through the body's system, are now thought to be the most detrimental type due both to their ability to lodge in the body and to the ensuing chemical exposures. As industry has followed EPA guidelines over the past several decades to reduce the total mass of particulate emissions, nanoparticle emissions may actually be increasing.[9] This fact has lead to a new focus on measuring not just the mass of particulate emissions but also the size distribution.

1.2 Particulate Sampling Methods

The desire to measure the size of particles and not just the total mass leads to the need for much more complicated techniques. While simple methods such as total filtering can be used to obtain total mass, dynamic instruments such as the scanning mobility particle sizer (SMPS) must be used to obtain size distributions as a function of engine operating parameters. The EPA has dictated several methods that must be used when measuring particle size distributions for compliance with regulations. These methods include not only the actual measuring instrument, but also a collection and dilution system to allow the instrument to obtain accurate readings.

The collection and dilution system used is so important because a particle size distribution at the exhaust manifold is not indicative of the distribution at the tailpipe or downstream of the vehicle. As the exhaust stream cools and dries, particles can collide and condense, growing either by collision or by mass accumulation. Because of this fact, an understanding of the time and temperature history of the particles is vitally important for interpretation of size distribution measurements.

1.3 Constant Volume Sampling

One EPA method for particulate emissions measurement simply samples exhaust at the exit of the tailpipe of a vehicle on a dynamometer. This method, while recreating mixing conditions, requires a full vehicle dynamometer, which is prohibitively too large and expensive for everyone but the large automakers. For experimental work at a smaller scale, and with individual engines, a different solution is desirable to be used. A method

developed by Kittleson and co-workers at University of Minnesota, is to use a miniature dilution tunnel to allow only a portion of the exhaust gas to dilute and cool.[17] This method has the advantage of being compact, but it does not necessarily reproduce the environmental conditions correctly.

1.4 Miniature Dilution Tunnel

A miniature dilution tunnel like the one used in this research allows a high-speed exhaust sample to decelerate and mix with clean, temperature controlled air. The dilution air can be controlled to adjust the dilution ratio, and to mimic different environmental conditions. A typical miniature dilution tunnel in operation at conditions suitable for testing spark ignition engines, must slow a flow with a Reynolds number of approximately 20,000, to a laminar flow with a Reynolds number of 900. This complex slowing and mixing process coupled to an unsteady engine obviously is not a steady phenomenon. Scanning particle size instruments such as an SMPS often require significant time to measure the particle size distribution, during which any variance in the flow characteristics can have an impact on the particle size distribution measured. The unsteadiness of the dilution system and the effects of turbulence and Brownian motion all may cause the particle size distribution to change.

1.5 Objectives

In the following chapters a series of experiments are described that look inside the dilution system and attempt to understand how these different phenomenon effect the measured size distribution. Analytical methods based on turbulent flow theory and

particle kinematics are also used to estimate how the particles may flow through the system. Finally, a numerical based Monte Carlo simulation is used to predict how individual particles move through the system. This work thus has a bearing on operation and use of dilution tunnels for particulate measurements from engines.

CHAPTER 2 Literature Review

2.1 Particulate Emissions

Recent studies have found that particles with a diameter of less than 2.5 microns carry the majority of health risks associated with aerosol particles.[2] These smaller particles are more apt to deposit inside the respiratory tract.[9] New engines designed for low particulate mass emissions have shown an increase in nanoparticulate emissions, or PM2.5, particles with a primary dimension smaller than 2.5 microns. For example a comparison of a 1988 and 1991 model diesel of the same model showed that while the new model had lower amounts of overall particulate emissions, the new model had higher levels of sub-100 nm particles.[2]

2.2 Sampling Standards

Exhaust sampling can have important implications on particle measurements. The EPA dictates in its “PM-10” standard for measuring particulate matter smaller than 10 micrometers that sampling probes have an efficiency of at least 50%. This means that in a representative sample no more that half the particles in any particular size are lost.[3] To achieve this for PM2.5, iso-kinetic sampling, ensuring that the velocity through the sampling probe is equal to that of the exhaust stream, should be used. This method should theoretically achieve a 100% efficiency, but particle loss due to impaction and diffusion to the walls on the sampling probe walls decreases this number for the largest and smallest size fractions of PM2.5 respectively.

2.3 Particulate Dynamics

The dilution tunnel design used in this research for this work is based on research completed by Kittleson and associates at the University of Minnesota.[17,18] The goal of the design is to mimic the environmental conditions that exist outside the tailpipe of a car inside laboratory conditions. Engine particulate matter can grow due to several phenomenon. Coagulation results from two particles hitting each other due to their random motion, sticking together and therefore creating a new larger particle. Coagulation is responsible for creating medium sized (2.5 um to 100 nm) particles and reducing the number of ultra fine particles.[5] Nucleation is the spontaneous creation of very fine (less than 100 nm) particles due to supersaturation and reaction inside the exhaust stream. Condensation occurs as the exhaust stream cools, and vapor changes phase either homogenously or on existing particles. Condensation can therefore be responsible for growth of both ultra fine and medium sized particles.

A typical particle size distribution from engine emissions exhibits a bimodal

Figure 2.1 Typical Size Distribution

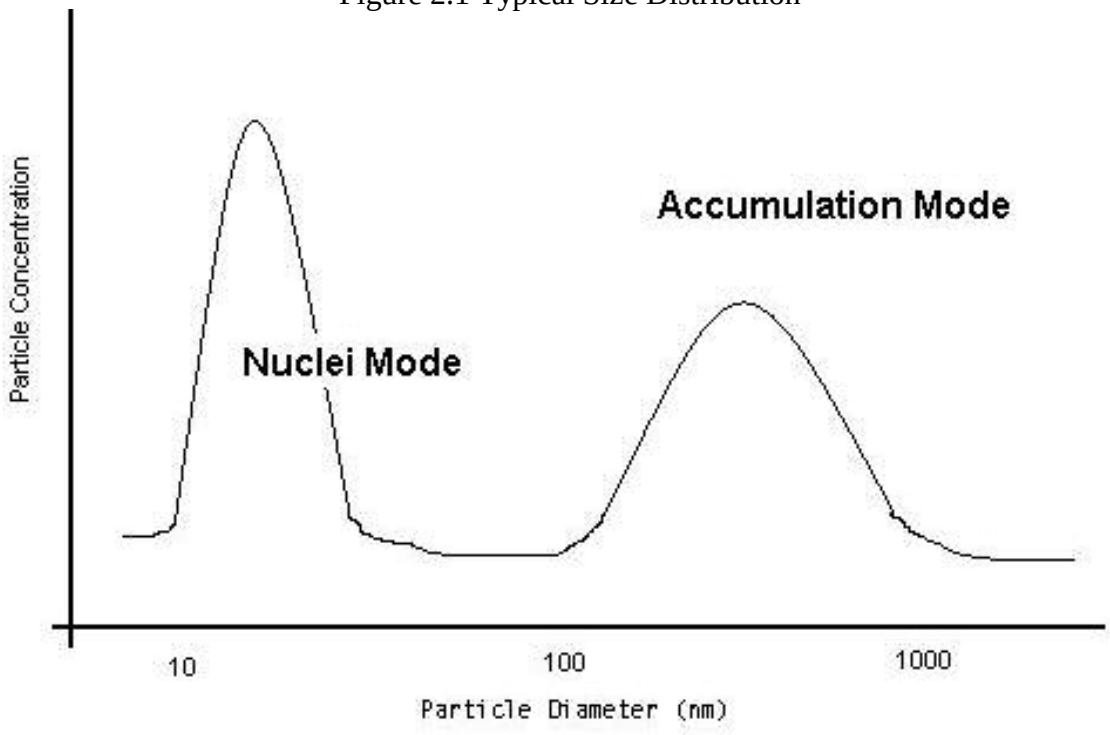

distribution as shown in Figure 2.1. The smaller mode is due to condensation and nucleation of particles, while the larger mode is primarily due to coagulation or break up of course particles.[5] Residence times for nanoparticles is on the order of minutes, while on the order of days for particles greater than 5 microns.[5] A change in residence time inside the tunnel of only half a second can decrease the particle count by a factor of five for nanoparticles particles. The same change in residence time has negligible effects on larger micron-sized particles.[18]

Over the range of these residence times, particle growth and decay is controlled by a number of factors. Coagulation can be enhanced by the turbulent motion of the flow or by high temperatures, which increases the rate of Brownian motion. Condensation is controlled by the temperature history of the flow as well as the chemical composition and humidity. All of these factors were addressed in Kittleson's dilution tunnel design. [17]

Experiments have shown that the dilution ratio, or volumetric change in concentration, under highway conditions varies linearly with residence time and distance from tailpipe. Approximately one second after leaving the tailpipe, particles are diluted to a ratio of 1000:1.[8] Kittleson's experiments and those described here attempt to duplicate a one second time history. Numerical and experimental work was completed on Kittleson's tunnel design that showed that laminar flow inside the tunnel was insufficient to fully mix the sample.[17] Turbulent flow, and in some cases wake disks to enhance the sample mixing, were found to ensure a uniform dilution ratio at the exit of the tunnel. Flow modeling using a K-ε model was used to determine dilution ratios with different configurations. It was found that in all cases with turbulent flow, the sample was fully mixed further than 1 meter downstream.[17]

2.4 Dilution Tunnel Optimization

A separate dilution system used at Massachusetts Institute of Technology was found to create complete mixing of the sample after a distance of nearly 2.8 meters and residence time of half a second.[7] The system studied at MIT was similar in design to Kittleson's with a longer geometry and smaller tunnel diameter. Temperature effects were also studied at MIT by measuring the sample's temperature at various points along the system. It was concluded that for lower flow rates and higher dilution ratios the final sample temperature was decreased. One concern when selecting flow rates and dilution ratios is to ensure that the final sample temperature complies with EPA regulations and is below 52 degrees Celsius. Optimum dilution ratios were studied at MIT with the goal of balancing the effects of higher residence times with lower dilution temperatures. A dilution ratio of between 13:1 and 18:1 was determined to be optimal for repeatability in the MIT dilution system. This conclusion was reached based on a sensitivity analysis of the effect of a small change in the dilution ratio on particulate readings. However, this conclusion did not take into consideration replication of real world environmental conditions.[7] Kayes and his associates also believe that when dilution temperature is independent of dilution ratio, dilution ratios above 15:1 will not result in relative changes in size distributions. They correctly state that at high dilution ratios effects of agglomeration are negligible, a valuable assumption.

2.5 Numerical Simulations of Dilution Systems

Numerical calculations were used to determine the flow characteristics inside a full flow dilution tunnel at the University of West Virginia.[6] A standard K-Epsilon turbulence model was used to study the turbulent sample jet mixing with the slower dilution air with and without mixing plates. These numerical calculations took into account the possibility of recirculation zones and mixing dynamics, but not particle dynamics and Brownian motion. The study determined that mixing plates in fact cause the flow to mix more rapidly and decrease the distance that the jet core propagates down the tunnel. Unfortunately these calculations were done on a full-scale tunnel and have limited application to a partial flow miniature system.

2.6 Analytical Approach to Free Jets

Even when the sample can be considered fully mixed at the downstream end of the dilution tunnel, each particle has a unique time history. The flow inside the tunnel can exhibit large turbulent eddies or recirculation zones that may entrain small particles and increase their residence times. Free turbulent jets are a well studied flow that can be described with analytical techniques. Analytically a free jet exhibits a self-similar solution, meaning that the centerline velocity, U(x), of the jet is proportional to the inverse of the axial distance from the origin. [1,13]

$$\frac{U(x)}{Uj} = \frac{B}{(x - x_0)/d} \qquad 2.1$$

Where Uj = initial velocity in the core of the jet

x = axial distance downstream

d = diameter of the jet initially

B = empirically determined constant.

This relationship and proportionality constant, B, are independent of Reynolds number. The spreading rate of a free jet can also be calculated from the following relationship:

$$r_{1/2} = (x - x_0)S \qquad 2.2$$

Where, $r_{1/2}$ = the radial distance to the half velocity

S = constant.

The velocity decay constant, B, has been determined to be 6.0 and the spreading constant, S, has been determined to be 0.097 by a number of different sources.[1,13] The normalized fluctuating velocity at the centerline of the jet decreases as one over the axial distance just as the mean velocity does. These relationships provide insight into the initial stages of high-speed jet decay, before the effects of the confining walls begin. For the flow rates inside the dilution tunnel this is only applicable for an x/d distance of about 10.

Another similarity solution for free jets shows that the centerline velocity decays according to a different relationship at x/d distances of more than 50. At the downstream end of the jet the centerline velocity decays as:

$$\frac{U(x)}{U_j} = C\left(\frac{x - x_0}{d}\right)^{-1/2} \qquad 2.3$$

Where, C = experimentally determined constant.

The experimental constant C, can be related to the turbulent Reynolds number and the momentum flux through the jet.[4] From these relationships and a suggested value for the Reynolds number, C can be fixed at 0.695. A comparison of these two relationships for centerline velocity, along with empirical data from confined jets can be seen in Section 4.5.

2.7 Experimental Work on Confined Jets

While the previously mentioned relationships can give a general view of how the jet will behave in a dilution tunnel, a large amount of experimental work has been done on confined jets that may give much more relevant insight. Coaxial confined jets have been studied heavily for applications in pipe design and combustor flow. Empirical data has shown that a confined jet generally decays slower and spreads less than an equivalent free jet.[19] Confined jets are primarily independent of Reynolds number, but can be effected by the step ratio, ß, which is defined as the ratio of the downstream diameter to the upstream diameter.[14,15] By adding the wall boundaries to the flow the simple spreading action of jet creates back flow and recirculation zones which are largely a function of the step ratio.[15] A detailed comparison of the various empirical results with data from this thesis is presented in Section 4.5 and shows that for axial distances less than 50 diameters Pope's correlations is well suited, and further downstream Bernard's solution provides better results.

CHAPTER 3 Apparatus Setup

3.1 Engine Dyno Setup

The overall setup of the dilution system is based on the recommendations of Kittleson et al in their paper "Single Stage Dilution Tunnel Design."[17] Several changes were made as noted below, in an attempt to increase the accuracy of readings.

A four-cylinder spark ignition GM Quad Four 2.0 liter engine is used as the source for the particulate emissions. A Dynaflow digital data logger continuously reads temperature and pressure sensors in a variety of places including manifold, oil and exhaust. Equivalence ratio is determined with an ECM 2400 series air-fuel recorder. The engine is connected to an electro magnetic dynamometer, which allows torque and speed to be maintained much more precisely than a typical water brake setup. All of the instrumentation is controlled from a PC running Dynaflow's software, linked to the apparatus via a local area network.

3.2 Dilution System

The exhaust is routed from the cylinder head via a specially made header, which runs approximately 2 feet into a 5 inch diameter exhaust pipe. The particulate sample is taken 6 feet downstream of the exhaust ports with a ¼ inch stainless fitting, aimed upstream in the center of 5 inch exhaust pipe. The exhaust is then vented outdoors. Stainless steel Swagelok™ fittings are used in all connections between the exhaust sample pipe and the particulate sampling device. The sample travels 6 inches through unheated but insulated lines to the mixing venturi. At this point, clean temperature and humidity controlled dilution air is sent into the venturi, creating a partial vacuum that

draws the exhaust sample into the venturi mixing the two streams. Figure 3.1 shows a simplified block diagram of the entire dilution system. Appendix A contains more detailed drawings of the apparatus.

The dilution air is supplied by a 5 HP commercial air compressor that sends the high-pressure air through a cooler and series of dryers and filters. This setup ends with a positive filtration of 5 nm particles. The air leaving this filter should be moisture and particle free and at room temperature. The high-pressure air from the filtration system is sent to a pressure regulator, and through Eomega digital flow meters. This allows the flow rate to be set quite precisely. The dilution air is then sent into a 14 inch length of heated pipe controlled by Love Controls Series 2600 temperature controllers. The sensing element for the controller is a thermocouple placed in the center of the dilution

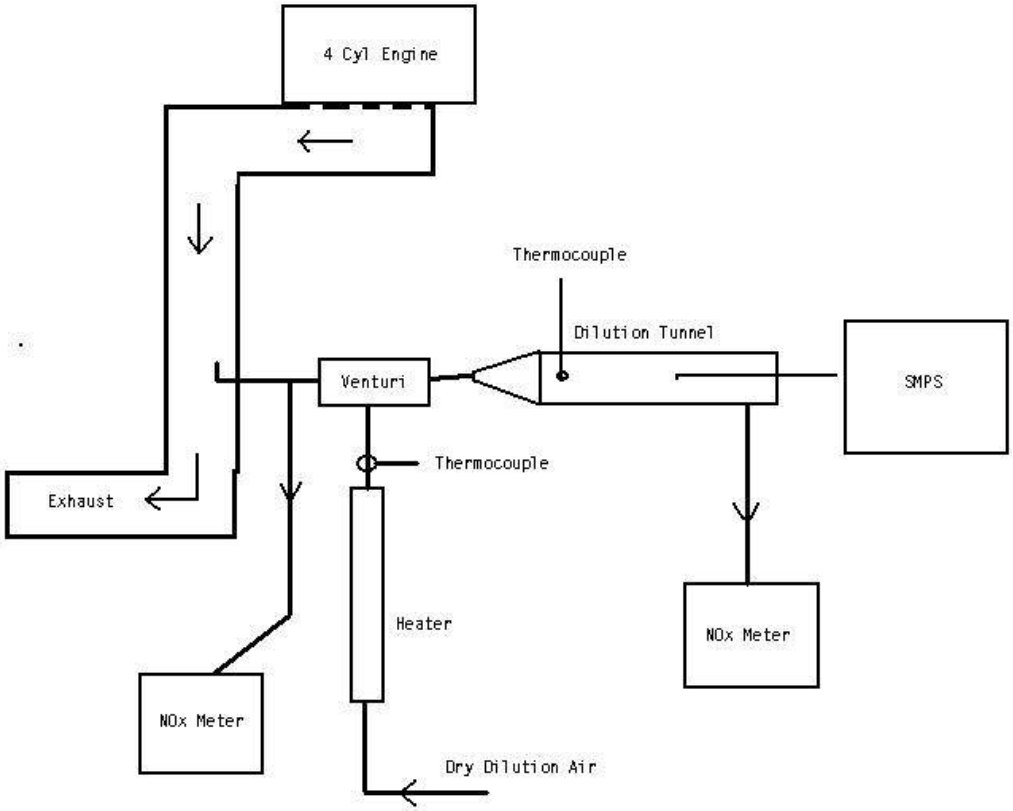

Figure 3.1 Dilution Tunnel Block Diagram

tunnel 25 cm downstream of the mixing venturi.

From the mixing venturi the diluted sample travels 15 cm to the entrance of the dilution tunnel. Here the ¼ inch pipe transitions into a 3 inch diameter tube at the centerline of the larger tube. The dilution tunnel is constructed of stainless steel with a ¼ inch wall thickness. To help eliminate any temperature gradients inside the tunnel, it is wrapped in insulation over its entire length. The tunnel comes apart in two places to allow cleaning and geometry changes. At both joints a plastic gasket and a five-bolt flange are used to ensure a positive seal. At the top of the tunnel three ¼ inch pipe thread ports are drilled though the wall to allow a variety of probes to be inserted; one of these ports is used to insert the temperature-controlling thermocouple. At the downstream end of the tunnel a ¼-inch Swagelok™ fitting allows a stainless pipe to slide back and forth in the axial direction. This pipe is connected to the SMPS via electrically conductive tubing to draw the sample from the tunnel. The rest of the diluted sample is exhausted through ¾ -inch plastic tubing to the atmosphere.

To determine the exact mixing ratio a series of nitrous oxide meters are used. A primary sample of exhaust is taken from the exhaust pipe near the sampling tube. A second sample is taken at the exit of the dilution tunnel. Both samples are sent to a Eomega NOx meter. By varying the dilution airflow from 10 to 60 liters per minute, dilution ratios of between 10 to 40 can be achieved.

3.3 SMPS Operation

The TSI model 3936 Scanning Mobility Particle Sizer consists of a differential mobility analyzer (DMA) and a condensation particle counter (CPC). The DMA and

CPC are computer controlled via a stand alone laptop computer. The DMA draws a vacuum of 1.5 liters per minute and helps to draw the sample from the tunnel into the classifier. At this point the polydisperse aerosol passes through a Kr^{85} radiation source, which gives the aerosol particles a known charge distribution.[16] The polydisperse flow is then passed down the cylindrical classifier tunnel, which has a grounded wall and a charged wire at the center. Depending on the potential of the wire, particles acquire a radial velocity, and for a particular potential particles of a known charge-to-mass ratio will exit the classifier and pass to the detector. This instrument has a number of auxillary settings such as sheath flow, scanning rate and impactor size, which are all managed by the computer using the supplied software.[16] Appendix A contains a detailed diagram showing the layout of the DMA.

The CPC detector counts individual particles using laser scattering. The monodisperse aerosol passes over a heated pool of n-butanol, and is then cooled to allow condensation on the particles. This allows nano-sized particles that scatter too little light to be detected to grow into micron-sized particles, which scatter appreciable light The TSI model 3022 CPC used has a minimum particle detection diameter of 7nm, which is smaller than the lowest range of particles filtered by the DMA.

The combined DMA and CPC allows a highly accurate particle size distribution to be recorded for particle diameters between 10 and 800nm. Unfortunately, it takes 150 seconds for the DMA to scan over the entire range of particles. During this length of time, transient conditions in the rest of the sampling system can cause problems with repeatability of results.

3.4 Dilution Tunnel Model

Besides the aforementioned experimental setup, a number of other instruments were used to investigate flow conditions inside the apparatus. An acrylic replica of the dilution tunnel was constructed so that visualization and laser Doppler Velocimetry (LDV) could be performed. The replica is made out of 3/8 inch clear acrylic and was of the same interior dimensions of the actual tunnel. Swagelok™ fittings are threaded into the entrance of the tunnel to allow existing hardware to couple to the model. The model is designed in two pieces to allow mesh screens to be inserted to help mix the flow.

3.5 Flow Visualization Setup

For the flow visualization experiments smoke was generated with a custom built heating device. An 8 inch coil of high temperature Nichrome wire was inserted into a ¾-inch PVC pipe fitting. The wire was connected to two car batteries in series to allow short pulses of 20 amp current to rapidly heat the coil, which is coated in mineral oil to generate smoke. The PVC fitting was threaded to accept Swagelok™ fittings so that the whole setup could be put in line immediately upstream of the tunnel model. This allows the flow to be relatively uninterrupted by the smoke generator, and minimizes the time for the smoke to diffuse before it reaches the model. The PVC fitting can be easily unscrewed so that mineral oil can be swabbed onto the wire coil between each firing of the smoke generator. Using a current pulse of less than one second produces a solid slug of white smoke, which travels out of the generator and into the Plexiglas model. The flow travels a length of 8 inches, or more than 60 diameters, between the smoke

generator and entrance of the tunnel allowing a normal turbulent velocity profile to redevelop.

A high-speed digital camera and computer were used to capture the rapidly mixing flow inside the tunnel. To show the small scale eddies with clear definition, a shutter speed of 1/1000 of a second was used, necessitating a very strong light source. To obtain a picture without excessive glare, a 2.5 kWatt spot lamp was put at the exit of the tunnel to light the setup in the axial direction. Barndoor shades and black paper were used to affect a very dark picture when no smoke was present, but as soon as the smoke entered a very well defined white cloud appeared on the camera. The visualization experiments used the actual dilution tunnel air supply and flow control. To study the effects of a temperature gradient between the flow and tunnel walls, a near infrared heat lamp was used to heat the acrylic to approximately 180 degrees Fahrenheit prior to some experiments.

3.6 Laser Doppler Velocimetry

The Plexiglas model was also used in conjunction with a Dyntech model one-dimensional LDV. The Dyntech laser head was mounted on a Dyntech 3D electronic transverse. Both the LDV and transverse were controlled by software running on a 486-class computer. The flow control system was a pressure regulator and Eomega digital flow meter as before, but using shop air as the supply. The regulated air was sent via Swagelok™ fittings to a 2 inch diameter plastic cylinder, which contained seeding particles. Titanium dioxide powder with a nominal diameter of 100 nm was entrained in the airflow by simple shaking of the seeding cylinder. The 3D transverse was set up so

that the two laser beams crossed through the Plexiglas at a right angle in the center of the model. The beams were then moved in a radial direction to allow the LDV to sample a slice of the flow field. Eighteen different radial positions were sampled from the wall to slightly past the center of the tunnel. Fifteen different axial positions were selected from

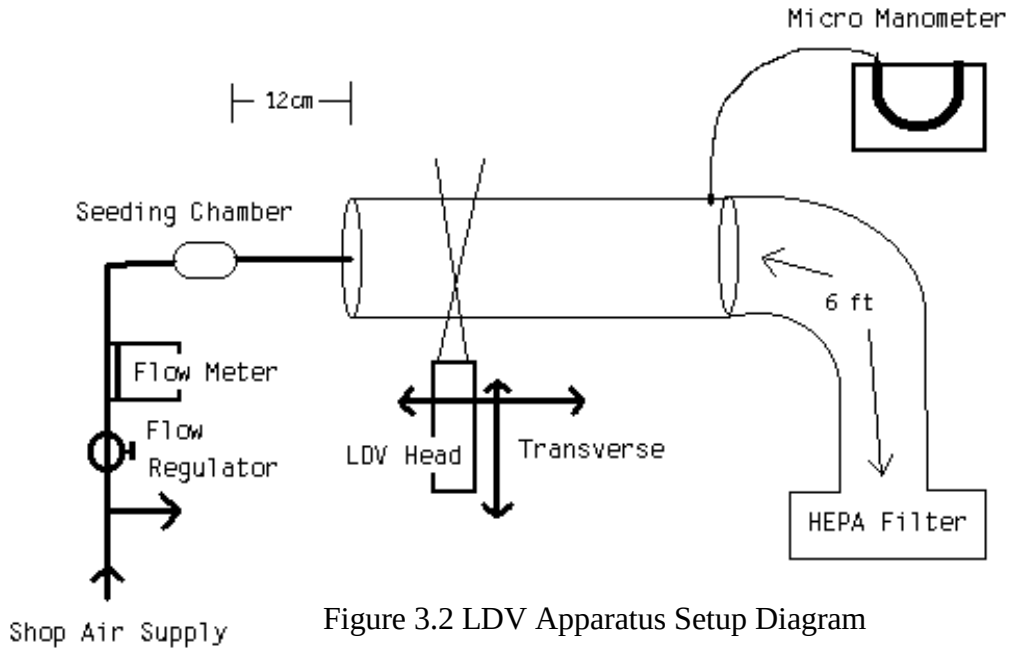

Figure 3.2 LDV Apparatus Setup Diagram

the entrance of the tunnel to 35 cm downstream. To eliminate the hazards of venting the titanium dioxide aerosol to the room, a HEPA filter was used to collect the powder four feet downstream of the exit of the tunnel. Six inch diameter ducting carried the flow from the tunnel to the filter to help eliminate any errors caused by adding the filter. A pressure tap and micro manometer were inserted at the exit of the tunnel to determine the pressure drop from the ducting and filter.

3.7 Temperature Probe

To investigate temperature effects inside the dilution tunnel a special eight-thermocouple probe was constructed. This probe consists of a piece of ¼-inch stainless tubing cut so that 9 separate thermocouples protrude on one side, equally spaced along the length of the probe. A Swagelok™ fitting was added so that the probe could be inserted into any of the ¼-inch pipe thread holes in the dilution tunnel and so that the probe could be positioned a different radial distances within the tunnel. Temperatures were recorded with the DynaFlow recorder from the engine, and then sent to the computer over the LAN. This system allows a real time picture of the temperature gradient in the flow between the wall and centerline of the tunnel.

3.8 NOx Concentration Experiment

Another experiment to investigate the flow and residence time inside the tunnel involved sending a slug of nitrous oxide calibration gas down the apparatus and measuring the concentration at various points downstream. This was accomplished using a Cambustion real time NOx meter with a resolution of 1ms. The dual probe instrument was set up on the existing dilution tunnel with one probe to measure the concentration at the mixing venturi, and a second probe that was positioned at various axial and radial positions.

3.8.1 Straight Tube Geometry

To first determine the feasibility of using real time NOx measurements to determine residence time and to experimentally determine the diffusion constant of the

NOx, the two-probe instrument was set up on a 27 inch length of straight 1/8-inch diameter stainless tubing with T fittings at each end. An electronic solenoid valve was used to switch between NOx gas and compressed air. Using pressure regulators the flow rates were equalized with the solenoid valve in both positions. The valve was rapidly

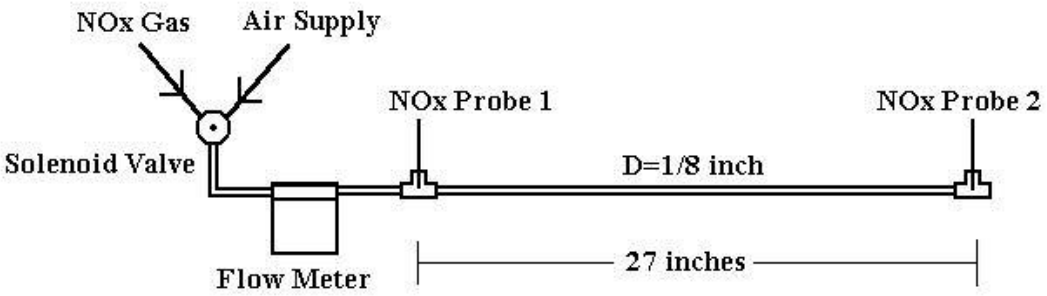

Figure 3.3 Straight Tube NOx Setup

tripped to allow a small slug of NOx calibration gas to pass down the tube. The concentration of Nox at both probes was recorded using an oscilloscope and downloaded to a PC computer. This was run for flow rates in the laminar, transition, and turbulent regimes. By measuring the time between concentration spikes in the two probes verses bulk fluid motion, diffusion constants can be determined for the calibration gas, and the diffusive effects of turbulence can be seen.

3.8.2 Tunnel Geometry

The NOx probe was then transferred to the actual dilution tunnel. Again pressure regulators were used to synchronize the flow rates of both the calibration gas and compressed air. The concentration readings were recorded with an oscilloscope and saved to a computer file. A single input flow rate of 15 liters per minute was selected, while the downstream NOx probe was placed in a variety of radial and axial positions.

At each position measurements were taken using both very short, 200 ms, and long, 5 seconds, tripping of the solenoid valve.

3.9 Pressure Measurements

To determine if pressure pulses from the opening and closing of the exhaust valves in the engine affected the flow conditions of the dilution system, pressure transducers were inserted at several downstream positions. A sensitive 10 bar pizo-electric pressure transducer was first calibrated and then inserted immediately before the mixing venturi, and 23 cm down from the entrance to the dilution tunnel. The engine was allowed to warm up and run at several typical test conditions. The output of the pressure transducers was recorded and saved using a digital oscilloscope and compared to the engine speed.

3.10 Generated Aerosol Size Distributions

A final experiment involving the dilution system and SMPS was used to attempt to correlate the effect of probe axial distance and flow conditions with measured particle size distributions without the uncertainty introduced by the engine and dynamometer. In place of the engine, a TSI model 3075 Constant Size Aerosol Generator was used to create the particulate flow. This piece of equipment atomizes a solution (here, sodium chloride) and dries it to yield a lognormal size distribution of stable particles. Depending on the flow conditions through the atomizer and salt concentration of the solution, a variety of size distributions can be

Figure 3.4 Aerosol Generator Setup Block Diagram

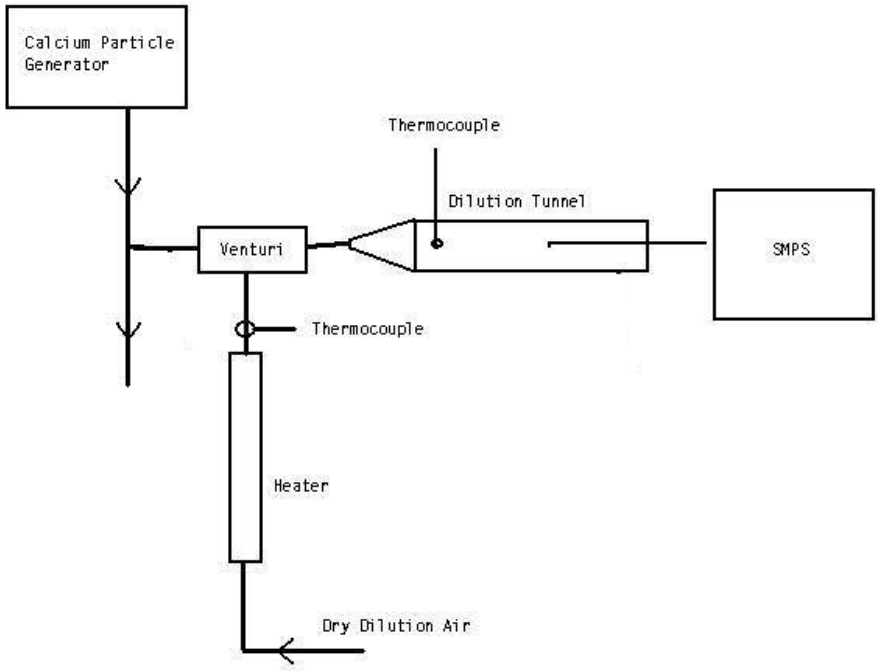

created. To pump the salt solution into the atomizer a variable speed electronic hypodermic needle pump was used. A pressure regulator connected to the existing compressed air supply was used to supply the airflow through the atomizer. The output of the atomizer was pushed through electrically conductive tubing to minimize the charge build up on the particles into a custom-built particle dryer. The dryer utilized Dryrite granules inside a 1.5 inch diameter pipe. The center of the pipe is kept open with a small metal screen, which allowed the wet aerosol to flow axially through the pipe while excess water was absorbed by the granules. From the exit of the dryer the aerosol enters the mixing venturi in the dilution system via statically conductive tubing again. This setup effectively replaced the exhaust sampling tube with a known, reproducible aerosol input. The SMPS was used to first read the size distribution of the aerosol directly from the dryer, and then at several different probe positions inside the tunnel with a known dilution ratio.

CHAPTER 4 Experimental Results

The experiments described in the previous section are all designed to gain knowledge of the fluid and aerosol dynamics operating inside the dilution system. The flow through the system is an unsteady turbulent mixing flow, which makes simple analytical analysis difficult. The experimental methods described in Chapter 3 are used to determine the flow characteristics.

4.1 Pressure Fluctuation Measurements

One of the defining characteristics of the flow in the dilution tunnel is its unsteadiness. Because the flow is created by a four cylinder engine operating at various speeds, the flow from the exhaust manifold consists of a series of pressure pulses. Each pulse corresponds to the opening of the exhaust valve and the exhaust stroke of one cylinder. The exhaust manifold combines these rapidly alternating pulses of gas into a single flow with a fluctuating velocity and pressure field.

A series of pressure transducers inside the dilution system coupled, with amplifying and recording devices allow the examination of the pressure fluctuations. The voltage reading on the recording oscilloscope can be converted to an relative pressure with an equation determined during transducer calibration. Based on the engine speed during these experiments a theoretical pressure wave can be calculated. Because the engine is a four stroke four cylinder, the time between each opening of an exhaust valve can be related to the engine speed by Equation 4.1.

$$\frac{pulses}{\text{sec}} = \frac{1}{30} \cdot rpm \qquad 4.1$$

The undamped pressure fluctuations can be represented by a sine wave with an arbitrary magnitude. The period of the sine wave then becomes one over the number of pulses per second based on engine speed. This ideal pressure function is included on the following figures to provide a baseline for comparison.

Figure 4.1 shows the pressure readings for the transducer located immediately after the mixing venturi. Also shown is the theoretical pressure pulse from the engine

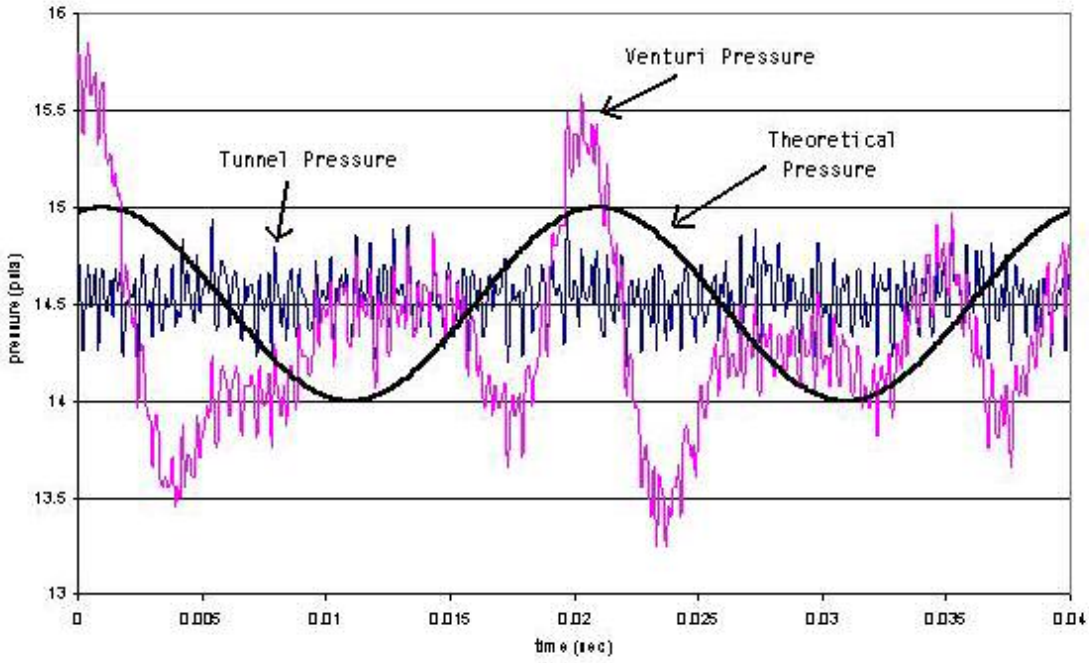

Figure 4.1 Pressure Fluctuations at Venturi and Tunnel

based on engine speed. It is interesting to compare the period of the sine wave to the spacing between experimental pressure pulses. It is evident that the exhaust manifold and 5 feet of exhaust piping have served to significantly smooth out the pulses. But a pressure differential of 1.5 psi is still apparent before the mixing venturi.

Figure 4.1 also shows the pressure readings from the transducer 23 cm downstream in the tunnel with the engine running at 1500 rpm. It is evident that by the time the fluctuating exhaust flow is diluted in the mixing venturi and starts to slow down in the dilution tunnel the pressure fluctuations have been largely damped out. Figure 4.2 overlays the pressure fluctuations at the venturi for several different engine

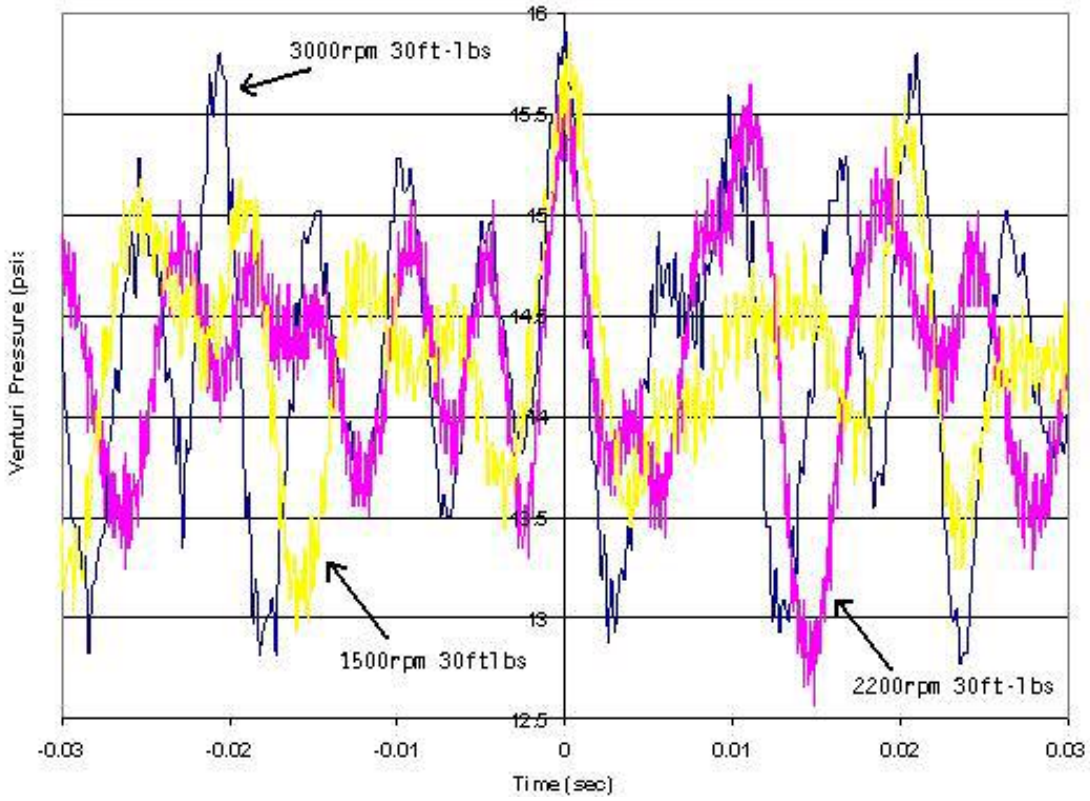

Figure 4.2 Pressure Fluctuations at Venturi at Several Load Conditions

speeds and loads. From this figure it is evident that even under a wide range of operating conditions the pressure fluctuations are similar to those in Figure 4.1. Under all of the test conditions the highest pressure fluctuations inside the tunnel were no more than 0.4 psi. This pressure fluctuation can be normalized with the stagnation pressure of the flow by:

$$P_0 = \frac{1}{2}\rho \cdot \overline{U}^2 + P_\infty \qquad 4.2$$

Where, ρ = fluid density

U = mean fluid velocity

P_∞ = far field pressure

P_o = Stagnation Pressure

At even the lowest flow test condition the pressure fluctuations turn out to be only 2.5% of the stagnation pressure, suggesting near steady state flow.

4.2 Temperature Gradient Measurements

At low velocities such as those present in the dilution tunnel, buoyant forces can induce significant fluid flows. The buoyant forces are directly related to the temperature gradient present in the flow. To determine whether this is an important factor in the dilution system, an experiment was devised that involved taking temperature readings simultaneously over a range of radial positions in the tunnel. The special 9 thermocouple probe described in Section 3.7 was used to measure temperature as a function of time and radial position while the system was warming up. This also facilitated the determination of the precise amount of time needed for the temperature controllers to bring the system to steady state after being turned on. Figure 4.3 shows the temperature of all nine thermocouples verses time after startup. After 26 minutes the system reaches steady state, with each of the thermocouples within 1% of their temperatures at infinite time. At this point, even with the tunnel wrapped in insulation a significant thermal gradient exists. Based on the temperature at tunnel center and the temperature at the wall, a

gradient of 0.32˚C (0.57 ˚F)

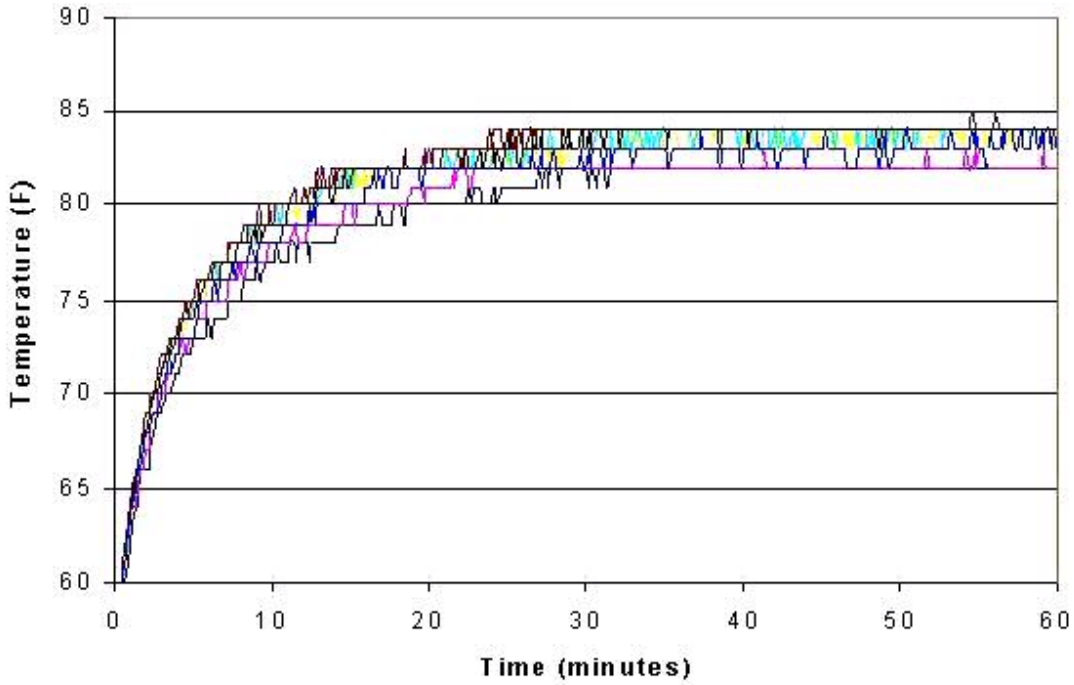

Figure 4.3 Temperature Probe Measurements vs Time

per centimeter exists. To evaluate how important this gradient is in the flow the nondimensional Grashof number can be used. The Grashof number is defined as:

$$Gr = \frac{g\beta(T_s - T_\infty)L}{u^2}\left(\frac{uL}{\upsilon}\right)^2 \qquad 4.3$$

Where, Gr = Grashof number

β = coefficient of thermal expansion

Ts = wall temperature

Tinf = temperature at tunnel center

L = characteristic length

u = fluid bulk velocity

υ = kinematic fluid viscosity

The Grashof number quantifies the ratio of buoyant forces to viscous forces in the flow. If Gr/Re^2 is greater than unity, the buoyant terms must be taken into consideration. For this experiment the Grashof number may be rewritten as:

$$Gr = \frac{g\beta(dT/dr)}{u^2}(\mathrm{Re}_d{}^2) \qquad 4.4$$

Where, Re = Reynolds number of the flow

dT/dr = thermal gradient

For the temperature gradient inside the tunnel the Grashof number is in fact 5.49 times Re^2 based on the bulk fluid velocity. This means that temperature effects may create some significant buoyant forces if the velocity does slow down to the bulk velocity. Despite this analysis, thermal effects will prove to be insignificant in Chapter 5, primarily because the Grashof number was calculated using the ideal bulk fluid velocity. In reality the fluid is traveling much more quickly than the bulk velocity because the jet in the center of the tunnel persists over much of the length.

4.3 Laser Doppler Velocitmetry

To determine the fluid flow velocity inside the tunnel, one dimensional Laser Doppler Velocimetry (LDV) was used with a clear Plexiglas model of the dilution tunnel. [LDV uses the fact that when a moving particle hits a coherent beam of light, it changes the frequency of beam slightly. By comparing two similar beams of light and looking at the interference pattern, the LDV instrument can determine the instantaneous velocity in

one direction. By sampling many instantaneous velocities the mean velocity of the flow can be determined as well as the standard deviation of the velocity distribution. These quantities can also show the relative intensity of turbulence inside the flow.

LDV measurements as described in Chapter 3 yielded a large amount of information about the flow. The volumetric flow rate was set at 15 liters per minute, and at each sampling point, and 1000 instantaneous velocities were recorded. This gave enough points in the velocity distribution to ascertain an accurate standard deviation and mean. At the beginning of each run and after changing the filter used to collect the seeding particles downstream, the pressure drop over the filter was measured. In most cases the pressure drop was around 0.02 inches of water, and at no time did it rise above 0.08 inches of water. This very small pressure is equal to less than 20 pascals or 0.23 m/s based on stagnation pressure. Using Matlab, the mean and standard deviation of the velocities were added to the spatial coordinates with respect to the entrance of the dilution tunnel. Figure 4.4 shows the resulting vector plot of the mean flow through the square geometry tunnel.

Evident in Figure 4.4 is the expected high speed flow at the center of the tunnel and gradual reduction of speed as axial distance increases. Also evident is a backflow along the wall and out to a radial distance of 20 mm. This is a recirculation zone caused by enclosing the turbulent jet. The recirculation zone does not exhibit the uniformity of the high speed jet. Instead, some portions of the backflow have stronger mean velocities than others. This shows a more complex flow than originally predicted by the free jet analytical solution from Chapter 2.

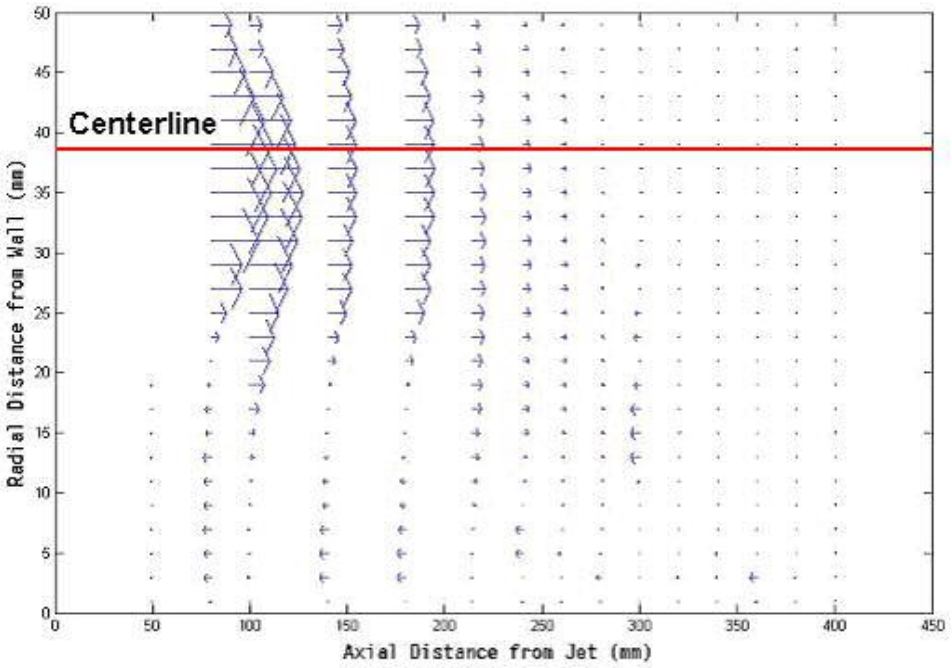

Figure 4.4 Mean Velocity Vector Plot, LDV Square Geometry

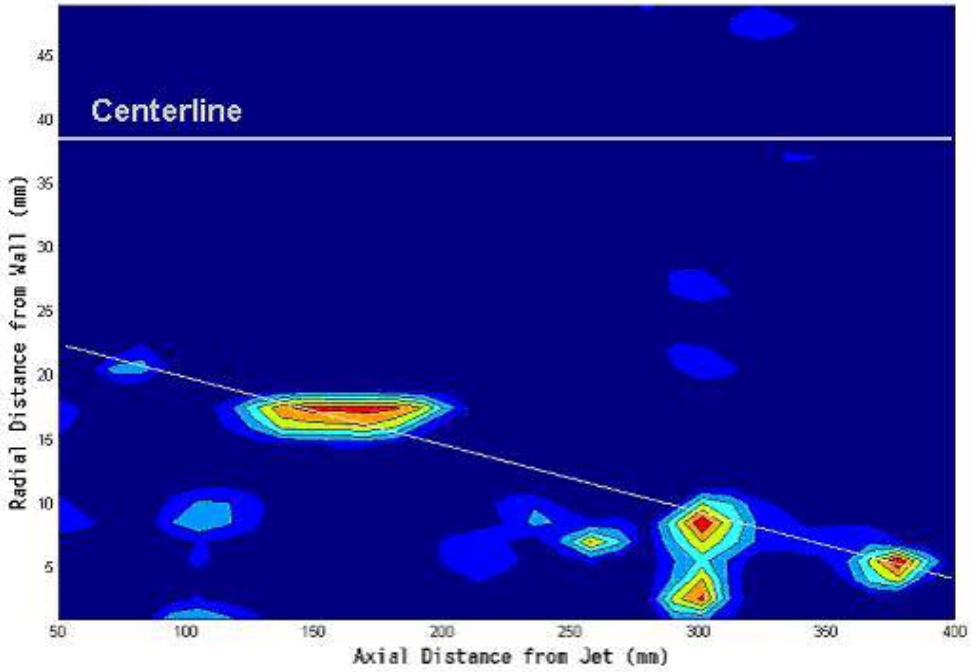

Figure 4.5 Turbulence Intensity Plot, LDV Square Geometry

The RMS velocity, turbulence intensity and standard deviation of the velocity distribution can be related by the following equation:

$$TurblenceIntensity = \frac{\sqrt{(u')^2}}{\bar{u}} = \frac{RMS}{\bar{u}} = \frac{\sigma}{\bar{u}} \qquad 4.5$$

Where, u' = instantaneous velocity

σ = standard deviation of the velocity distribution.

Figure 4.5 shows the normalized RMS velocity in the same spatial coordinates, illustrating the strength of the turbulence. As expected, the strongest turbulence exists at the entrance of the jet into the dilution tunnel. Other pockets of turbulence occur at decreasing radial distances from the tunnel wall, forming a nearly straight line as axial distance increases. This line of above average turbulence intensity corresponds to the shear layer where the backflow and the high speed jet intersect. In this region the normally small turbulent structures are mixed by the shear layer and overall turbulent intensity increases. These results are only indicative of the flow, however, because the LDV measures only velocity in one direction, while the flow is a complex three dimensional phenomenon.

The same experiment was done using the conical diffuser instead of the square geometry for the tunnel. Because a transparent diffuser was not available, velocity readings could only be taken downstream of the end of the diffuser. Figure 4.6 shows the vector plot of the mean velocities inside the tunnel downstream of the diffuser. The high speed jet is not present in the center of the tunnel, and is instead replaced with two separate regions. A backflow seems to exist towards the center of the tunnel, while the

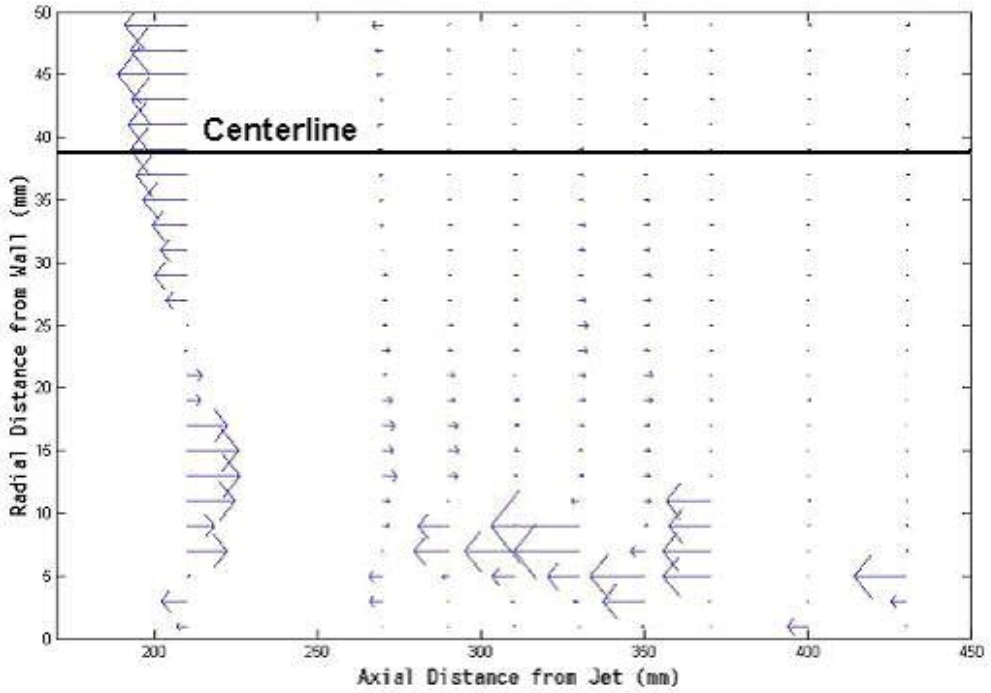

Figure 4.6 Mean Velocity Vector Plot, LDV Conical Geometry

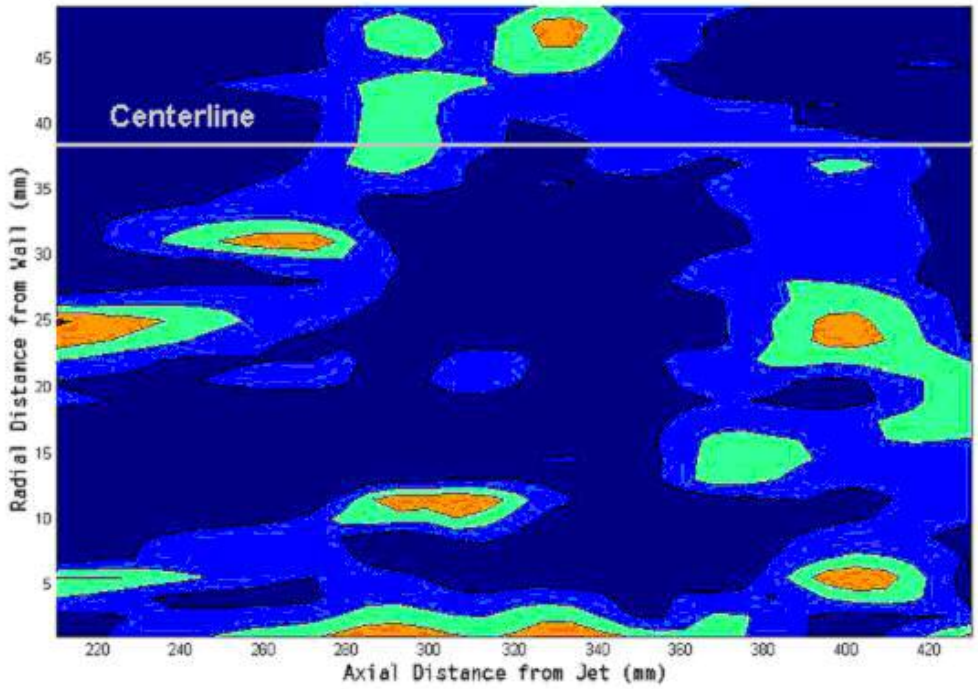

Figure 4.7 Turbulence Intensity Plot, LDV Conical Geometry

downstream flowing jet is closer to the wall. A large pocket of backflow exists along the wall slightly further downstream between x = 275 and x = 375 mm. The turbulence intensity, shown in Figure 4.7, shows the greatest intensity at the shear layers between the recirculation zones. Both of these figures seem to indicate a stalled diffuser. When a diffuser has too great of a divergence angle for a given flow rate, it can stall causing the flow to jet down one of the walls instead of staying centered. In this stalled condition a small perturbation can cause large, random fluctuations in the jet location. Initially the conical diffuser was built in the hopes that it would cause the jet to relamanarize more quickly following introduction of the engine exhaust into the dilution tunnel, but the LDV data shows that the opposite is in fact true. Instead the diffuser causes the flow to become less predictable and generates as large or larger back flow regions than the square geometry. For these reasons the conical diffuser was left out of most of the rest of the experimental procedure. The focus of this thesis will be on prediction of the flow only in the cylindrical tunnel geometry, because it is more useful in real-world situations.

4.4 NOx Experiment Calibration

Another method to gain information about the mixing dynamics inside the tunnel is to send slugs of NOx calibration gas through the tunnel, and measure the concentration downstream. Before this experiment (described in Section 3.8) was performed, the method was used on a straight piece of 0.187 cm diameter stainless steel pipe. Three different flow rates in the pipe were selected to yield flows in the laminar, transition and turbulent regimes. This experiment is intended to show how the NOx calibration gas diffuses not just due to molecular motion, but also from turbulent mixing.

Figures 4.8, 4.9, and 4.10 show the NOx concentration verses time for the three flow rates selected corresponding to a Reynolds number of 238, 2250, and 4416 respectively. At each flow rate three different length slugs of NOx were injected into the tube. It is evident from the comparison of the three plots that it takes a shorter time for the slug to travel down the pipe at higher flow rates. By integrating the concentration plots for each slug sent down the tube the total amount of NOx can be found. It is obvious even without integration, that the area under corresponding curves is not the same at the input and output of the tube, particularly in Figure 4.8. The lack of mass closure means that somewhere NOx is being lost. This loss is due to some of the flow being diverted into the actual NOx probe itself. In order for the probe to achieve sampling times as fast as 1 ms, the probe must sample at a very high flow rate. Even though the probe pipe diameter is less than 0.8 mm, the total volume flow rate is enough to affect the results of the experiment. To determine exactly how much of the flow is being diverted into the NOx probe the integrated areas of several concentration over time curves are compared. This comparison shows that a loss of 4.89 % occurs when the total flow rate through the pipe is 15 liters per minute, which means that the probe accounts for a total flow rate of 0.734 liters per minute. At all three measured flow rates, the probe will always draw this much sample and at the low flow rate of 2 liters per minute, this proves to be a significant portion of the flow.

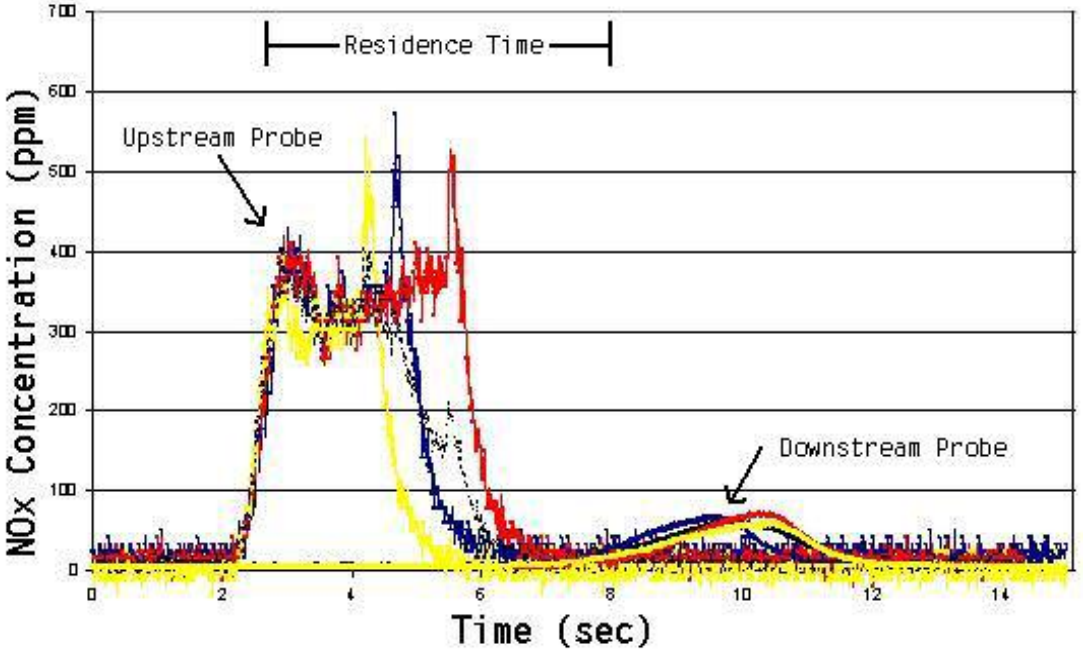

Figure 4.8 NOx Concentration Plot, Flow Rate = 1.5 l/min, Re = 238

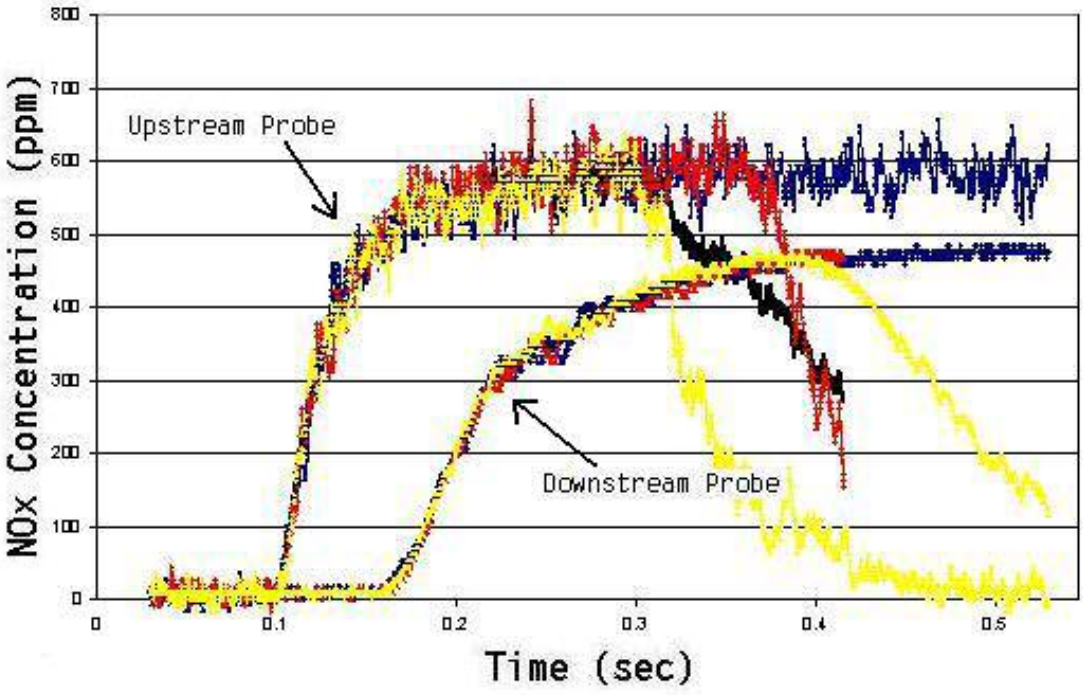

Figure 4.9 NOx Concentration Plot, Flow Rate = 8 l/min, Re = 2250

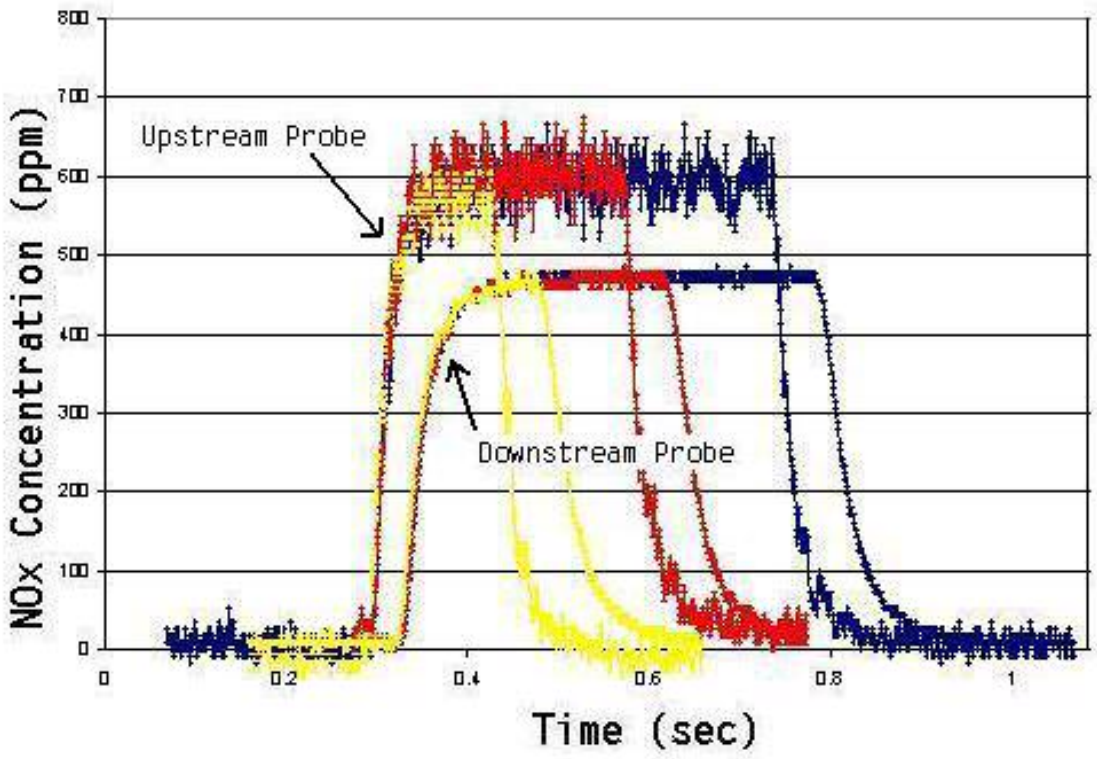

Figure 4.10 NOx Concentration Plot, Flow Rate = 15 l/min, Re = 4416

Table 4.1 shows the flow rates, velocities and corresponding theoretical residence times through the pipe, after correction for losses into the NOx probe. Also shown are the actual times recorded between the first increase in concentration at the two probes.

Volume Flow Rate (l/min)	2 l/min	8 l/min	15 l/min
Velocity (m/s)	0.7404	6.990	13.721
Reynolds number	238	2249	4416
dT theoretical (s)	0.9265	0.0981	0.0499
dT Experimental (s)	0.492	0.064	0.0276
Distance Diffused (m)	0.32173	0.2386	0.3073
Diffusivity Coef. (m^2/s/)	0.01596	0.032207	0.3086
Turbulence Intensity	0.14483	0.0618	0.1484

Table 4.1 Comparison of Residence Times and Diffusivity for Straight Tube

Based on the difference in actual and theoretical residence times, a value for the distance traveled through gas diffusion and turbulent mixing can be calculated. This calculation is shown in Equation 4.6.

$$DiffusionDis\tan ce = (\Delta T_{act} - \Delta T_{theo})\overline{U} \qquad 4.6$$

Where, $\bar{U}$ = mean bulk fluid velocity

ΔT = residence time

From this distance due to diffusion, a total diffusion coefficient can be calculated. Einstein's equation for diffusivity yields:

$$X_{rms} = \sqrt{2Dt} \qquad 4.7$$

Where, X_{rms} = root mean square distance traveled by the particle or molecule

D = diffusivity constant

t = time over which the phenomenon occurs

Brownian diffusion is random and molecular diffusion distances take on a Gaussian distribution with X_{rms} equaling one standard deviation. X_{rms} can be indirectly determined from Figures 4.8-4.10 by using the time until the concentration reaches half of the instead of using the time between the first probe and the start of the concentration rise in the second. Based on a Gaussian distribution the half maximum point is reached at 1.18 standard deviations. Thus a factor of 1.18 is divided out of Equation 4.7 when calculating the values of diffusivity in table 4.1. This total diffusion constant can be

broken up into diffusion due to molecular motion, and that due to turbulent fluid motion. [13]

$$D_{total} = D_{Brownian} + D_{turb} \qquad 4.8$$

It is obvious from Table 4.1 that the diffusion coefficient varies considerably between the laminar and turbulent flow regimes. This larger diffusivity is due to the added mixing, created by the turbulent motion.

From kinetic theory, the diffusivity constant due to molecular motion can be calculated from the following equation.[5]

$$D = \frac{1}{3}\lambda \cdot \bar{c} \qquad 4.9$$

Where, λ = mean free path of the gas

$\bar{c}$ = average speed of the molecules

This yields a diffusion coefficient of 2.99E-7 m^2/s for NO_2. This is significantly smaller than any of the diffusion constants in Table 4.1. This means that most of the gas diffusion and hence increased residence times are due to the turbulent motion of the flow. From this, a relative turbulence intensity can be calculated from the overall diffusivity coefficient. By taking the derivative of Equation 4.7 with respect to time the RMS velocity can be determined.

$$V_{rms} = \frac{\sqrt{2} \cdot D}{2\sqrt{D \cdot t}} \qquad 4.10$$

And the overall turbulence intensity is defined by:

$$I = \frac{\sqrt{(u')^2}}{\bar{u}} = \frac{V_{rms}}{\bar{u}} \qquad 4.11$$

From Equations 4.10 and 4.11 the turbulence intensities for the three different flow are shown in Table 4.1. As expected, the intensity is higher for the turbulent Reynolds number, than for the transitional Reynolds number. Both of these intensities are of the correct order of magnitude as well.[4] The high caculated turbulence intensity in the 2 l/min laminar flow is clearly in error, likely due to problems with a majority of the flow being diverted into the NOx probe. At a flow rate of slightly under 2 liters per minute, almost half of the flow is diverted into the first probe, causing a slower overall velocity in the tube. Then the second probe draws another 0.734 liters per minute, causing an inflow from the exit of the tube. All of this makes the measured residence time of the slug erroneous, leading to incorrect values of diffused distance and diffusivity coefficients for the laminar flow case.

4.5 NOx Experiment

The NOx sampling procedure allows quantification of the residence times and velocites in the actual dilution tunnel. The sampling probe was located at a number of axial positions downstream from the jet, and at several radial distances at three separate downstream positions. With the probe at each of these sampling points, three slugs of different duration were injected, allowing a comparison between three identical flow conditions. Figure 4.11 shows a typical plot of the deflection of these three different slugs at a sampling position 23 cm downstream of the jet, and at a radial position of 3.4 cm.

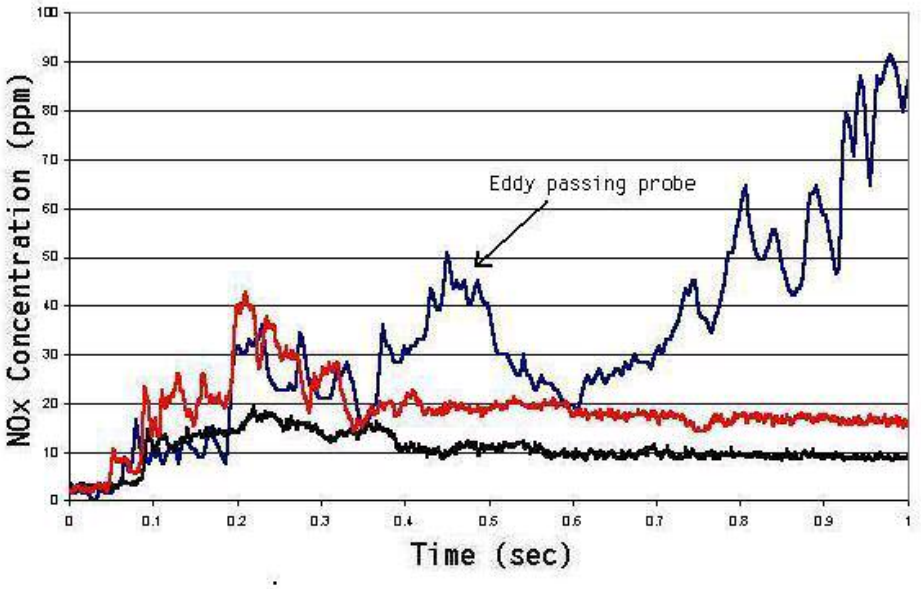

Figure 4.11 NOx Concentration Plot, R = 3.4 cm, x = 23 cm

Dissimilartities in the curves are evident. The total areas under the curves and overall magnitudes are expected to be different in each case, but the variation in the shape of the curves is unexpected. Instead of a constant increase in NOx concentration, as was evident in the previous experiment shown in Figures 4.8 - 4.10, there are peaks and local minima in the measured concentrations. The explanation for these irregularities is the

presence of turbulent eddies transporting the gas. As each eddy passes the sampling probe, it brings with it an increased and fluctuating concentration of NOx. Then as the eddy moves on, the probe is again sampling gas that is more dilute. The irregularities present in Figure 4.11 appear in the plots of NOx concentration at all sampling positions, but in various magnitudes. At locations further downstream, or nearer the tunnel centerline, the magnitude of the irregularities is much smaller. This pattern would seem to indicate that at positions near the tunnel centerline or further downstream, the eddy size is small. These observations are confirmed in Sections 4.6 and 5.3.

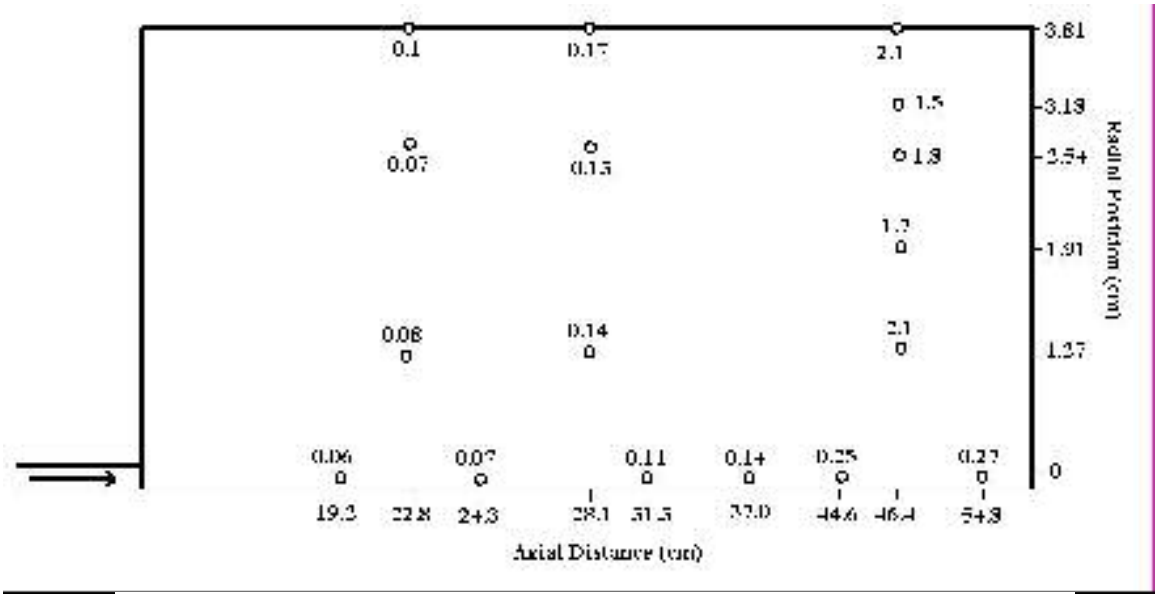

Figure 4.12 NOx Probe Positions and Calculated Residence Times

Although the concentration plots are dissimilar in shape, the initial increase in measured concentration occurs at nearly the same time at each sampling point. A mean residence time can be determined by qualitatively analyzing at each of these plots. Figure 4.12 shows the locations of the sampling points in relation to the tunnel geometry, along with the residence times. The residence times indicate that the flow is indeed faster

at the center of the tunnel as expected. Mean velocities are calculated, and correlated with a position halfway between the two sampling points used for the calculation.

Figure 4.13 shows the centerline velocities normalized by the jet speed based on the bulk flow rate, Uj, as a function of axial distance normalized with the diameter of the jet, d. Because of the limited number of data points, only a few centerline velocities can be calculated. Figure 4.13 also shows a number of empirical and analytical relationships for free and turbulent jets discussed in Section 2.6, e.g. both the $1/x$ and $1/x^2$ relationships for free jets are shown. Park's data is from an experiment which measured velocities within a co-flow jet., with the measurements were done with the jet flow set to twice the velocity of the co-flow.[12] Risso's experiments used a laser doppler system to measure a flow similar to the dilution tunnel, but with a closed end.[14] Step ratios as low as 0.22 were used with a Reynolds number of 22,000. This experiment closely matched the dilution system except for the outflow conditions. Yang's experiment was very similar to our dilution tunnel, except that their step ratio was fixed at a very large 2.7.[19] A Reynolds number of 64,000 was used, and detailed information about the turbulent intensity and Reynolds stress was recorded. Based on Figure 4.13, Yang's empirical data seems to fit the closest, even though his geometry included a very different step ratio. Yang's experiments yielded information about not only the centerline velocity, but also kinetic energy, turbulence intensity, and Reynolds stress. This information is compared to results from the LDV and numerical solutions in Chapter 5.

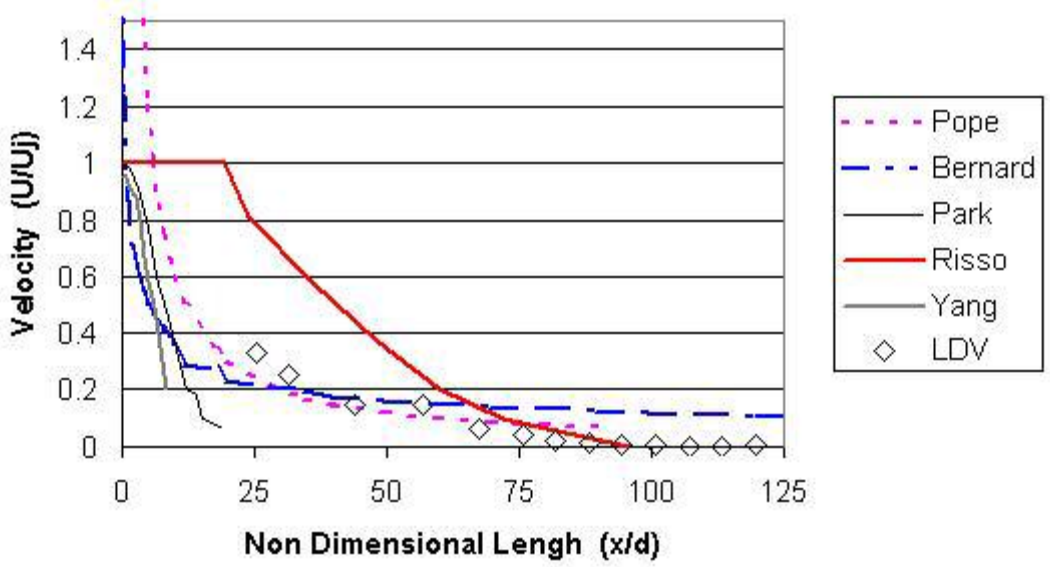

Figure 4.13 Non-Dimensional Centerline Velocity

4.5.1 Qualitative Turbulent Observations

A comparison of the concentration fluctuations can yield qualitative information about the turbulence. From examination of plots like Figure 4.11 from different probe positions, the time between fluctuations can be measured. It can be assumed that at larger times, larger sized eddies were present in the flow. From this assumption it is evident that along the centerline the eddies are small or nonexistent because the NOx plots exhibit very rapid and small fluctuations. From similar analysis of the NOx plots, at positions off center, the eddies are larger upstream than downstream. Both of these conclusions correspond with observations made in the following section.

4.6 Flow Visualization Observations

Utilizing the experimental procedure in Section 3.5, flow visualization experiments were conducted at three separate flow rates with different geometries. The jet spread and diffusion angle can be qualitatively calculated from the still images of the flow. Shutter speeds were high enough to capture the large eddy motions of the jet, and eddy sizes and speeds can also be measured from the still images. Figure 4.14 shows the captured still images of the jet for three different flow rates. A time of zero is equal to when the smoke first appears from the jet aperture. Because the dimensions of the tunnel and the time between frames are known, the jet spread angle and speed can be calculated, as shown for each of the flow rates in Table 4.2.

	15 l/min	30 l/min	50 l/min	15 l/min Screen
Spread Angle (deg)	4.83	6.91	6.10	5.75
Eddy Size (cm)	0.86	1.40	1.12	0.86

Table 4.2 Comparison of Spread Angle and Eddy Size vs Flow Rate

As evident from Figure 4.14, at higher flow rates the jet stays confined to a small diameter for a longer distance downstream, before diverging. When it then starts to diverge, the angle is greater at higher velocities. Comparison between the low flow rate with and without the mixing plate inserted at an axial distance of 19 cm shows that it does change the dynamics of the flow. The mixing plate causes a pressure drop in the flow, which backs up the flow slowing it and causing it to further diverge. Figure 4.15 shows the flow further downstream than Figure 4.14 with the time scale set so that zero time equals when the smoke front first enters the picture. Figure 4.15 can be used to

evaluate the extent to which the jet has slowed into a parabolic velocity profile expected in turbulent pipe flow. The addition of the mixing plate does not significantly improve the break down of the jet.

A comparison of the eddy structures evident in Figures 4.14 and 4.15 illustrate the complexities in the flow. As the jet spreads, large eddies randomly break off into the shear layer separating the jet from the back flow region. A higher speeds, these eddies are larger in size and move more quickly. Figure 4.15 shows that even further downstream, where a generally parabolic velocity profile is observed, eddies are still prevalent, forcing portions of the flow to surge ahead of the rest of the smoke front.

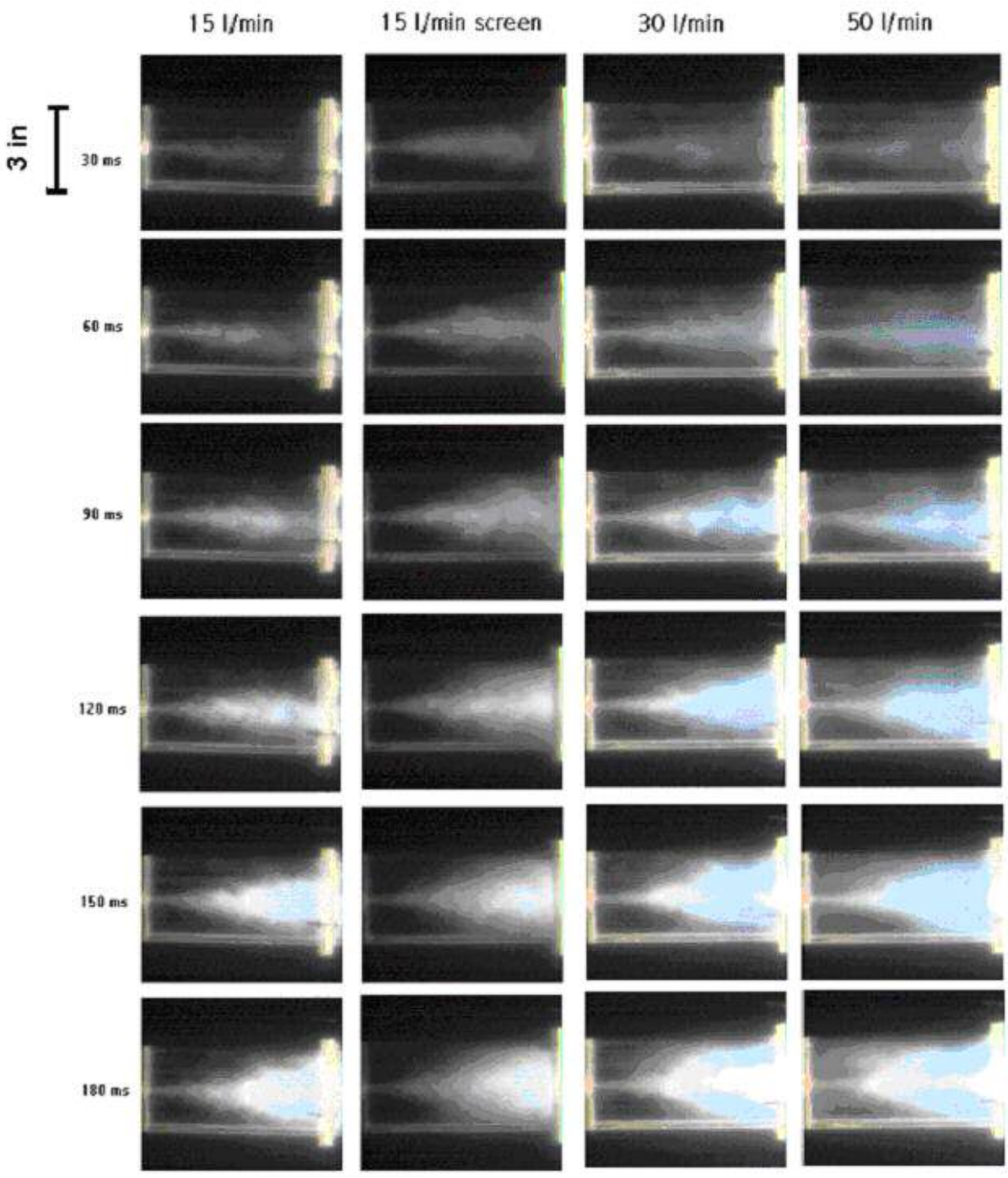

Figure 4.14 Captured Still Images from Flow Visulaization

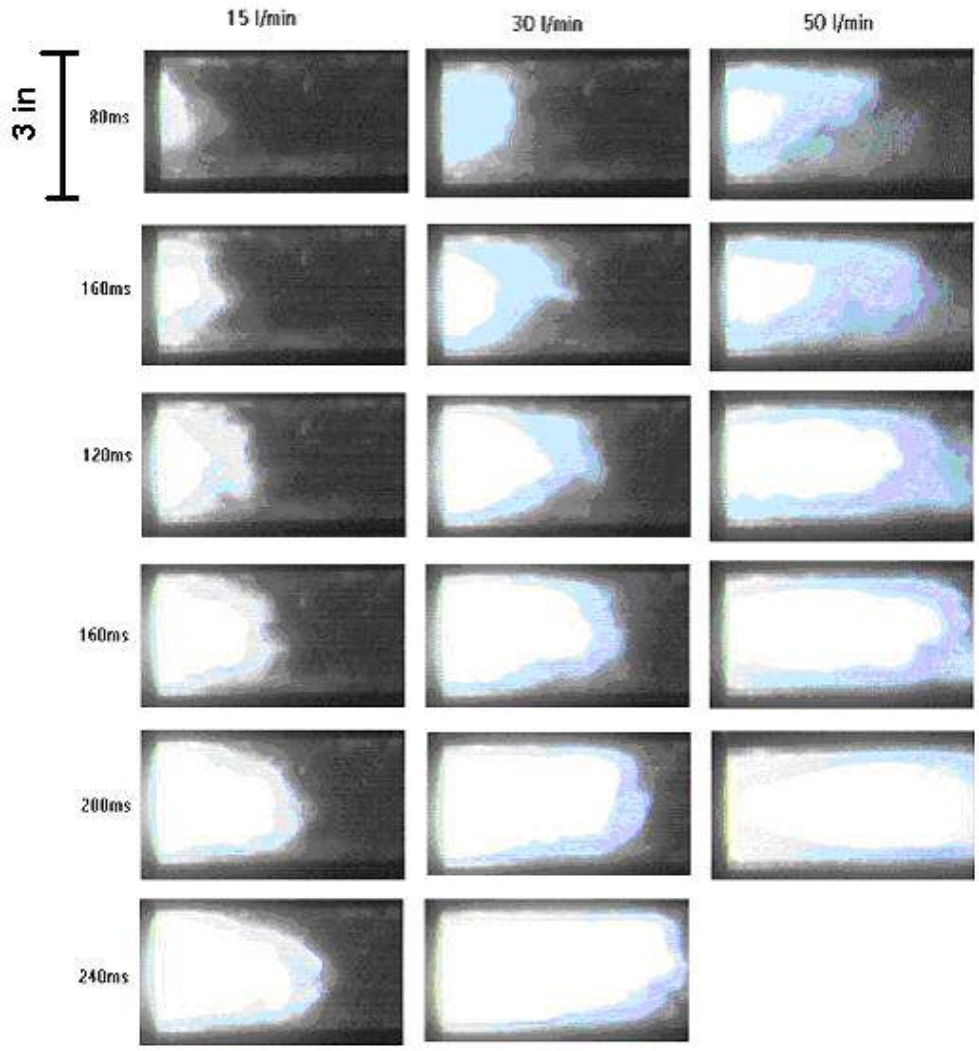

Figure 4.15 Captured Still Images from Flow Visualization Downstream from Figure 4.14

Although the visualization experiment yields mostly qualitative information, some important quantities can be measured. By measuring the distance the smoke front travels in a single frame, an estimate of the velocity can be obtained. Figure 4.16

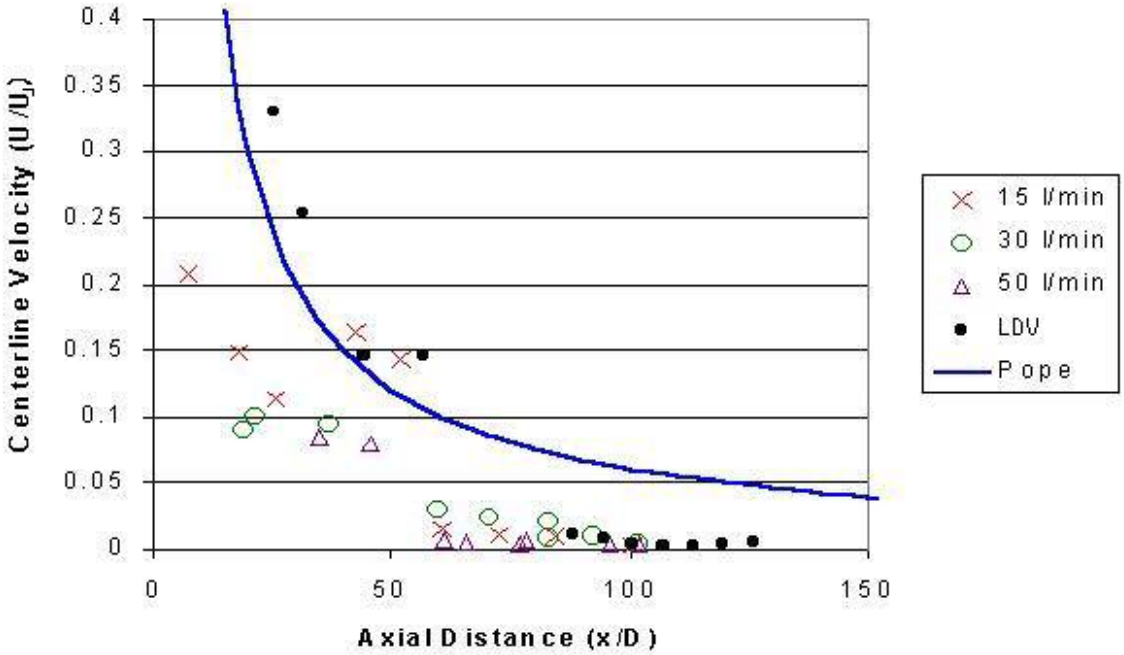

Figure 4.16 Centerline Velocities from Flow Visualization and LDV

shows these centerline velocities plotted in non-dimensional coordinates. Data from all three different flow rates is shown along with the centerline velocities acquired from the LDV in section 4.4. It is obvious that this rough data follows the general trend expected for confined jets outlined in Chapter 2.

4.7 Aerosol Generation Experiment

A constant aerosol source as described in Section 3.10 was used in conjunction with the SMPS to evaluate how probe position effects the measured output size distribution. Unfortunately only a small amount of data was obtained from this experiment before Hurricane Isabel flooded the laboratory, but it can still yield some insights into the particle dynamics.

Figure 4.17 shows the size distributions recorded from the SMPS over a scan time of 120 seconds. The other lines show the size distribution measured with the output probe at various axial positions. There is no positive trend between axial position and size distribution, although the

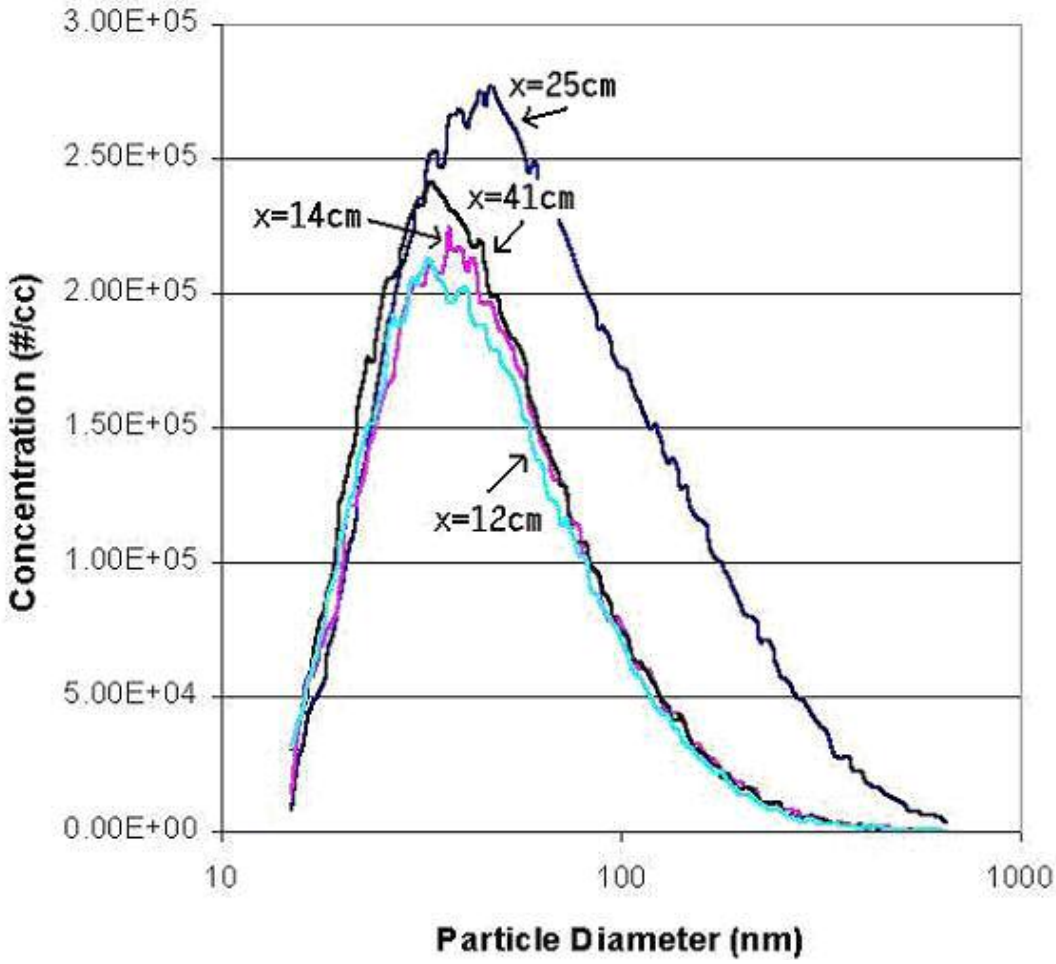

Figure 4.17 Particle Size Distribution at Various Axial Positions

results show that even small variations in position can affect the measurements. Observed variations in the particle size distribution with probe position provide motivation for numerical analysis in Chapter 5.

CHAPTER 5 Modeling

This chapter examines the flow and particle dynamics from an analytical approach, to determine correlations that may exist between model predictions and the experimental results from the previous chapter. The fluid flow through the tunnel is analyzed with a basic laminar bulk flow approach, with similarity solutions for turbulent jets, and finally with computational methods. Particle dynamics are investigated including the effects of Brownian motion and fluctuating velocities due to turbulence. Finally, all of these components are integrated using a Monte Carlo type simulation to estimate particle size distributions that may be measured at particular sampling points at the outlet of the tunnel.

5.1 Bulk Flow Analysis

The first step in analysis of the dilution tunnel flow is the determination of the magnitude of velocities and Reynolds numbers present in the apparatus. In the simplest incompressible bulk flow analysis, assuming that the flow instantly transitions from a high speed flow in the inlet pipe, to a slow speed flow in the tunnel, the velocities in the tunnel and inlet pipe can be related directly to the volumetric flow rate in Equation 5.1:

$$\dot{Q} = A_1 V_1 = A_2 V_2 \qquad 5.1$$

where, A_1 = area of the inlet

A_2 = area of the tunnel

Q = volumetric flow rate

V_1 = velocity in the inlet

V_2 = velocity in the tunnel

The Reynolds number (Equation 5.2) is typically used to determine whether the flow is laminar or turbulent. For Reynolds numbers above 2000, the pipe flow is typically considered turbulent.[10]

$$\mathrm{Re} = \frac{Ud}{\upsilon} \qquad 5.2$$

where, d = pipe diameter

u = kinematic viscosity

U = mean or bulk fluid velocity

Based on Equations 5.1 and 5.2 the following table can be constructed.

Flow Rate	15 l/min	30 l/min	50 l/min
Inlet Velocity, V1	33.7 m/s	63.3 m/s	107 m/s
Inlet Re, Re1	7491	13164	22347
Tunnel Velocity, V2	0.06 m/s	0.11 m/s	0.18 m/s
Tunnel Re, Re2	298	547	912

Table 5.1 Comparison of Flow Rates Using Bulk Flow Analysis

It is evident from these simple calculations that at all three characteristic flow rates, the Reynolds number is well into the turbulent region inside the inlet tube. While in the tunnel, the flow should exhibit laminar behavior if given an very long distance to relaminarize. Problems with this type of analysis exist because, as shown in the previous chapter, the flow does not laminarize over the distance of the tunnel. Instead the flow retains its turbulent characteristics over the length of the tunnel.

5.2 Free Turbulent Jets

To understand how the high speed turbulent flow in the inlet transitions to the larger area tunnel, two separate types of jets are examined. As discussed in Chapter 2, free turbulent jets can be described using self similar solutions. Bernard[4] and Pope[13] offer two different solutions for the centerline velocity of a free jet, given by Equations 2.1 and 2.3. Bernard and Wallace's book also offers some insight into the radial properties of free jets, suggesting that radial velocity profiles can be normalized with:

$$\bar{U} = U_c(1 - \tanh^2 \eta) \qquad 5.3$$

Here, $\bar{U}$ = mean velocity

U_c = centerline velocity

η = similarity variable

$$\eta = \frac{yR_t}{4x} \qquad 5.4$$

Where, x = axial distance

y = radial distance from centerline

R_t = experimental constant = 25.7

Figure 5.1 shows LDV data plotted in these non-dimensional coordinates, along with the expected velocities for a free jet calculated from Equation 5.3 and some radial velocity profiles taken from Yang at a Reynolds number of 64,000.[19] It is evident the radial

velocity profiles are similar in shape over a range of η values. The experimental data

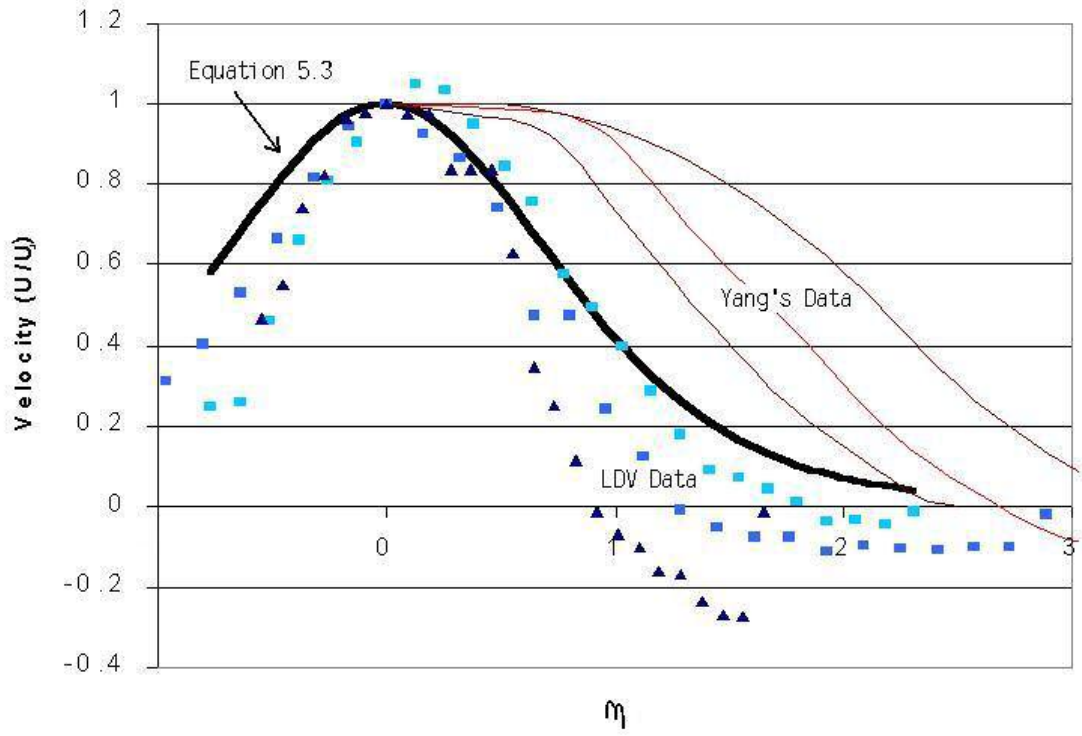

Figure 5.1 Radial Velocity Profiles from LDV data and Yang's Experiment

also takes a similar shape to the predicted profile, with only a difference in magnitude, which is expected due to the effects of the side wall boundaries verses the boundless flow of a free jet. The walls inhibit the divergence of the jet, with the result that at larger values of η, the velocities are smaller than predicted by Equation 5.3. Also absent in Equation 5.3 and Yang's data is the presence of a backflow region. This backflow measured using the LDV reveals itself in negative values of U/U_j.

5.3 Computational Methods

To further examine the tunnel flow, two different commercial computational fluid dynamics codes were utilized. First, ANSYS was used to solve the averaged Navier-

Stokes equations using a standard K-ε closure. Both isothermal and energy-dependent models of the tunnel were solved for the three flow rates corresponding to the experiments, i.e. 15, 30 and 50 liters per minute. Adding the energy equation to the solver did not affect the final solution at any of the flow rates, despite the calculated Grasshof number (based on the radial temperature profile as in Section 4.2) being larger than 5.8.

A second, more common code, Fluent, was used to solve the turbulent flow field for the tunnel geometry. Again a K-ε closure was utilized and isothermal conditions were assumed. Values for the K-ε closure constants were entered per Bernard's book and are as follows:[4]

$C\mu = 0.09$

$C_{\varepsilon 1} = 1.44$

$C_{\varepsilon 2} = 1.92$

$\Sigma k = 1$

$\Sigma e = 1.3$

After one solution was found to converge to acceptable tolerances, the mesh independence was checked by doubling the number of elements in the analysis. In both cases the solutions the centerline velocity decay was nearly identical. For the rest of the computations, a grid with 8900 unevenly spaced elements was used. The solution given by the Fluent solver yielded the

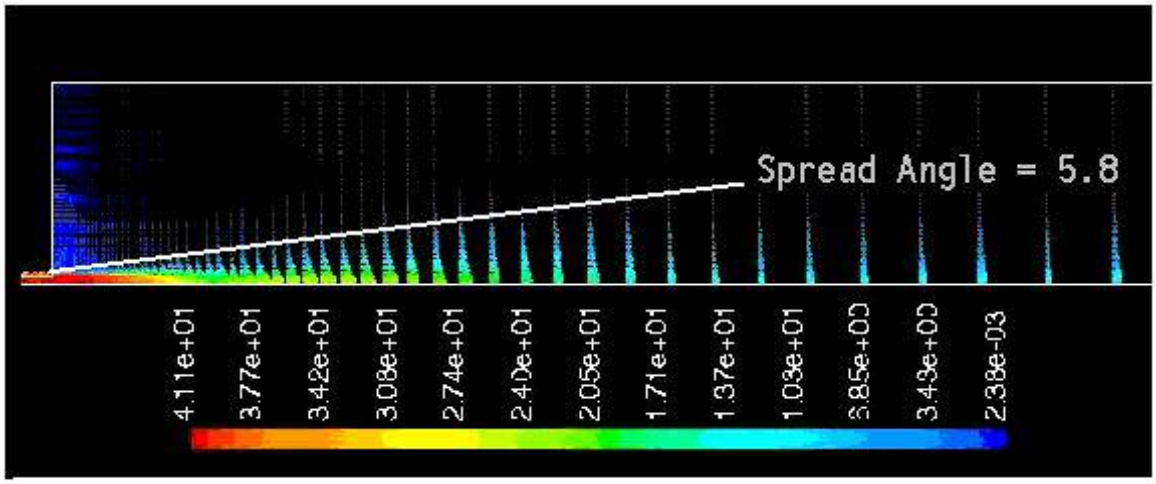

Figure 5.2 Mean Velocity Vector Plot from Fluent Solution, Flow Rate = 50 l/min

high speed jet shown in Figure 5.2, including a recirculation zone and back flow region, as expected.

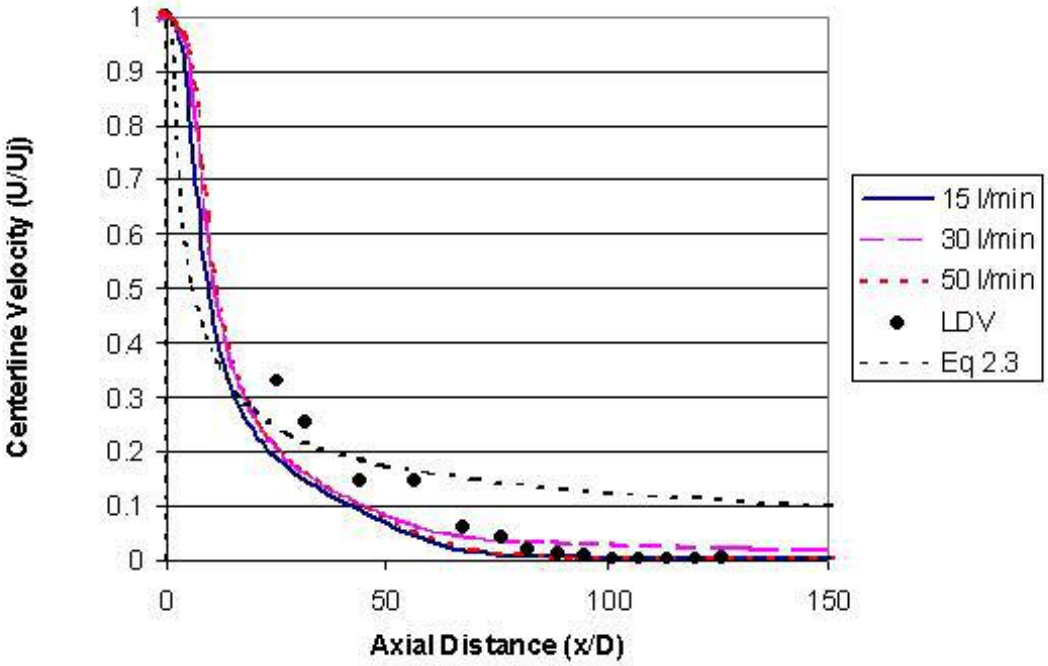

Figure 5.3 Centerline Velocity Comparison Between Fluent Solutions

A spread angle of 5.8 degrees agrees closely with the measured spread angle of 4.6 degrees from Section 4.5. Figure 5.3 shows the non-dimensional centerline velocities

from Fluent plotted alongside the experimental data from Chapter 4. It can be seen that the Fluent Model accurately predicts the centerline velocity for all three flow rates. The CFD code is sensitive to the number of cumulative iterations; with each iteration the solution is refined. At smaller numbers of iterations, the code predicts a very slow decay of the jet, and a backflow region that exists over the entire length of the tunnel. If the code is allowed to run further, the residuals tend to flatten out indicating a slow convergence of the solution. After several thousand more iterations, the backflow region

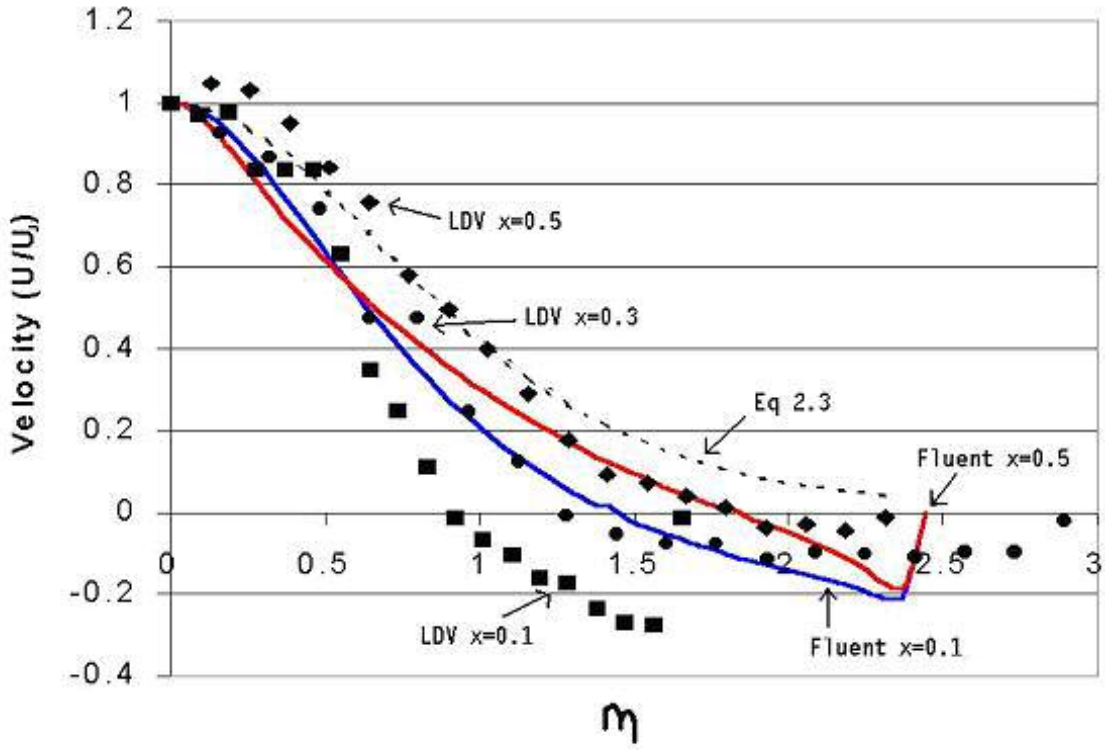

Figure 5.4 Experimental and Fluent Radial Velocity Profiles

at the end of the tunnel eventually disappears, and it is at this point that the iteration is stopped.

Figure 5.4 shows the experimental and modeled radial velocity profiles at several axial positions plotted in the nondimensional coordinates suggested by Bernard and

Wallace.[4] The profiles take on a similar shape for smaller values of η for both experimental data and analytical solution. Because Equation 5.3 does not take into account the enclosed jet and hence the back flow region, the profiles diverge at larger η values. From Figure 5.3, it can be concluded that the Fluent code does an acceptable job of predicting the mean velocity field inside the tunnel. The shear and back flow region measured experimentally are present in the Fluent predictions, but little quantitative comparison with experimental results can be done in these areas. Naturally, because the CFD code uses a Reynolds averaging closure, no information about the turbulent eddy motion is contained in the solution. This is a significant flaw that will be addressed in Chapter 6.

5.4 Brownian Motion

Brownian motion is the result of momentum imparted to molecules or particles by collisions with neighboring molecules or particles due to their natural Maxwellian velocity distribution. Because Brownian motion is statistically random, it can be described by a Gaussian distribution. The magnitude of this motion is heavily dependent upon the mean free path of the gas and the velocities of the particles. This in turn can be related to the temperature and pressure of the fluid, along with the characteristics of the particles in the fluid. Using kinetic theory to relate all of these quantities to a diffusivity constant, D, Einstein derived a formula for particles in Stokes flow.[3]

$$D = \frac{kTC_c}{3\pi\eta d_p} \qquad 5.5$$

Where, C_c = slip correction factor

k = Stephan Boltzman constant

T = temperature

η = gas viscosity

D_p = particle diameter

The slip correction factor can be calculated using the following formula.[5]

$$C_c = 1 + \frac{2\lambda}{d_p}(A_1 + A_2 e^{-A_3 d_p / \lambda}) \qquad 5.6$$

Where, A_1,A_2,A_3 = experimental constants

λ = mean free path of gas

d_p = particle diameter

The slip correction factor is important for submicron particles for which length scales are of the same order as the mean free path. For these particles the continuum assumption of the fluid breaks down, and the slip correction factor must be used.

After the diffusivity constant is determined for a particular sized particle, the RMS distance traveled by the particle over a time, t, can be calculated using another formula attributed to Einstein.

$$x_{rms} = \sqrt{2Dt} \qquad 5.7$$

Using Equation 5.7, the root mean square distance traveled by the particles due purely to Brownian motion was calculated for the flow in the tunnel. It was assumed that the flow behaves as in Section 5.1, as a bulk laminar flow, and that each particle would follow the streamlines exactly except for the influence of diffusivity. Figure 5.5 shows the RMS distance the particles diffuse for the 50 liter per minute flow rate in the square geometry and Figure 5.6 shows the conical geometry.

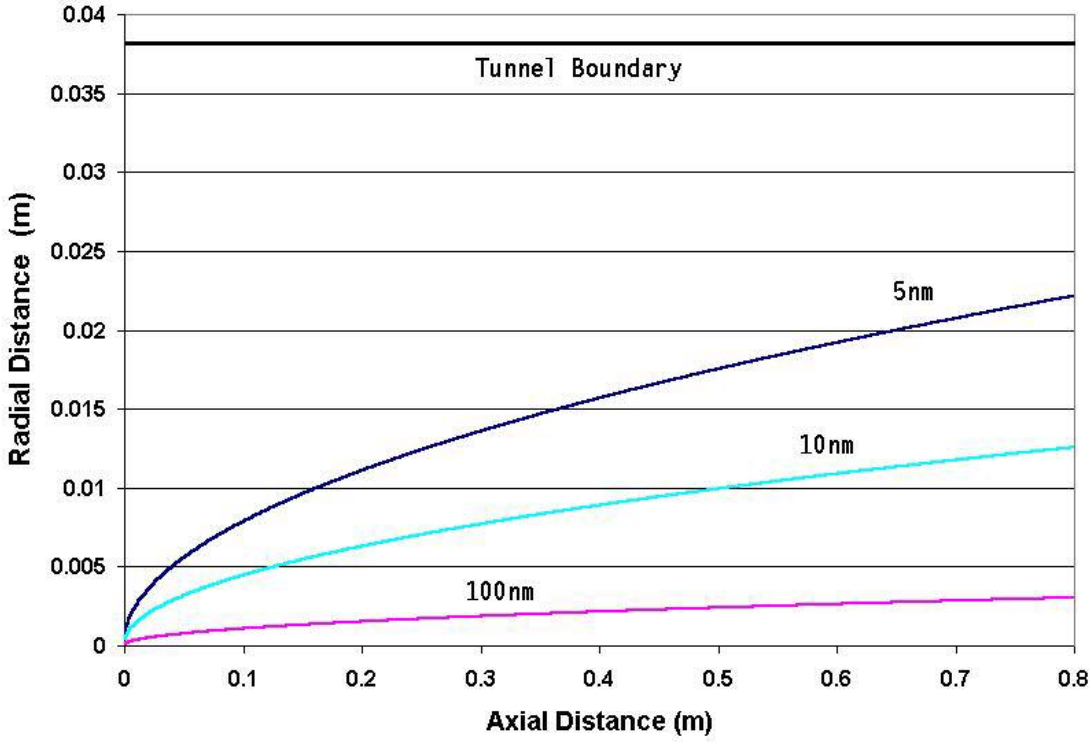

Figure 5.5 RMS Distance Diffused in Square Geometry, Flow Rate = 50 l/min

Decreasing the particle diameter by a factor of 20 increases the diffusion distance by roughly a factor of 8. Significantly, this means that the concentration of the sampled particles at a point will vary due to this diffused distance. This simple calculation shows that Brownian motion by itself will not adequately mix the dilute flow, and in fact stratifies the dilution ratio by particle diameter.

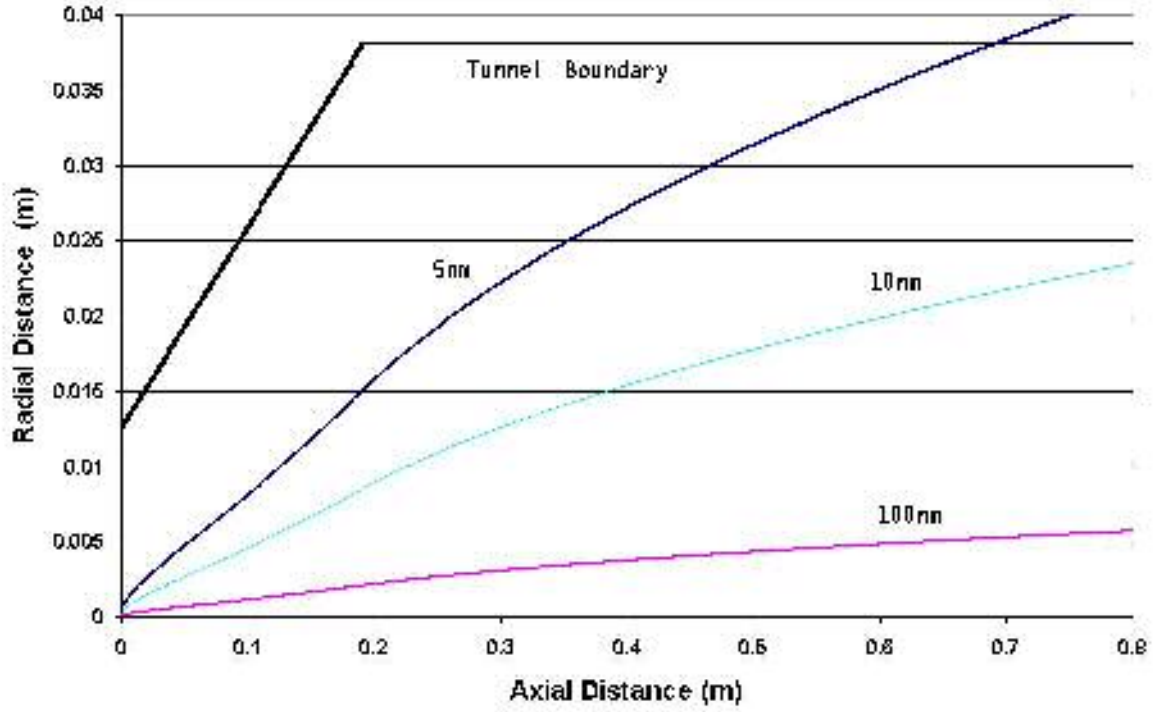

Figure 5.6 RMS Distance Diffused in Conical Geometry, Flow Rate = 50 l/min

In order to implement the effects of Equation 5.7 into any type of numerical simulation, it is helpful to know what the velocity distribution due to Brownian motion is, which can be accomplished by taking the temporal derivative of Equation 5.7.

$$V_{rms} = \frac{dx_{rms}}{dt} = \frac{\sqrt{2}D}{2\sqrt{Dt}} = \sqrt{\frac{D}{2t}} \qquad 5.8$$

With the root mean square of the velocity distribution known, a simple Gaussian random variable can be used to simulate Brownian motion.

5.5 Aerodynamic Particle Drag

Another important aspect of the particle dynamics is the determination of how well a particular sized particle follows the fluid streamlines. All particles are affected by drag forces due to the fluid velocities acting on them. The drag force on small particles , $Re_d < 1$, is described by Stokes' Law:[3]

$$F_{drag} = 3\pi\eta V d_p \qquad 5.9$$

where, V = relative velocity past particle

η = gas viscosity

d_p = particle diameter

At very small particle diameters ($d_p < 1$ μm, approximately) the Equation 5.9 does not hold, due to the breakdown of the continuum assumption, and an alternative must be used.[3]

$$F_{drag} = \frac{\pi C_d V^2 d_p^2}{8 C_c} \qquad 5.10$$

Here, C_c = Cunningham slip correction

V = relative velocity

and

$$C_d = \frac{24}{\mathrm{Re}}(1 + 0.0196\,\mathrm{Re}) \qquad 5.11$$

In Equation 5.11, Re = Reynolds number over the particle, and Re<5 [3]

From Equations 5.10 and 5.11 the drag force can be calculated in all three directions assuming the relative velocity past the particle is known. Combining the size dependent drag knowledge of the velocity field from the computational model, Lagrangian particle paths can be calculated as shown in Section 5.7. The Stokes number can be used to generalize dynamic behavior for a variety of flows and particle sizes. This non-dimensional number relates the particle stopping distance to a characteristic flow length and is important in the design of filters and impactors. First the stopping distance must be calculated: [3]

$$S = V\frac{\rho d_p^2 C_c}{18\eta} \qquad 5.12$$

Where, V = the particle velocity

ρ = particle density

S = stopping distance

The Stokes number is then simply:

$$Stk = \frac{S}{d} \qquad 5.13$$

In Equation 5.13, d = the characteristic dimension over which dynamic forces act on the particle. To determine if particles will follow the streamlines of the tunnel flow, the

Stokes number must be calculated for a given particle size and flow dimension. It is appropriate to set d equal to the turbulent microscale, which represents the smallest size of the eddies in the flow and yields a worst case Stokes number. Table 5.1 shows the various aerodynamic properties of several different sized particles including their Stokes number.

Diameter (nm)	5	10	50	100	500	1000
Slip Correction Factor	2.853	1.835	1.151	1.075	1.015	1.008
Diffusivity $x10^6$	134.6	43.3	5.43	2.54	0.497	0.238
Tau (sec $x10^6$)	0.0424	0.109	1.71	6.4	151	600
Stokes Number d = 1 μm	1.27E-04	3.28E-04	5.14E-03	0.0192	0.453	1.79
Stokes Number d = 53 μm	2.41E-06	6.21E-06	9.73E-05	3.64E-04	8.58E-03	3.39E-02

Table 5.2 Calculation of Stokes Number for Various Particles

In the calculation of Table 5.2, the particles were assumed to be made of carbon, and the Kolmogorov micorscale was used. The Stokes number for a Kolmogorov scale of one micron was calculated for the velocity field from Section 5.6. The second Stokes number was calculated using a Kolmogorov scale of 53 microns was used based on the tunnel geometry with a flow rate of 50 liters per minute. This microscale was calculated using the turbulent dissipation rate given by the Fluent solution from Section 5.3. It is evident that for particles smaller than a micron in diameter, the Stokes number is less than one, and thus these particles it can be assumed that their trajectories follow the streamlines exactly. In Section 5.7 the trajectories for low Stokes number particles are assumed to in fact follow the streamlines accurately.

5.6 Calculation of Particle Trajectories

Assuming that the velocity field can be accurately calculated, it is relatively easy to have a computer solve for particle trajectories based on a simple force balance. As previously shown in Section 5.5, a relationship for the drag force on a given particle in any direction can be found knowing only the particle diameter and relative velocity of the fluid past the particle. Using Newton's second law, neglecting gravity and surface tension forces for nearly neutrally-buoyant particles:

$$\sum F_i = m\frac{\partial V_i}{\partial t} = F_{drag\,i} \qquad 5.14$$

Here, m = mass of the particle

V_i = the relative velocity of the fluid in the i direction

F_i = the drag force in the i direction

Equation 5.14 can be broken down into separate x and y direction equations, assuming the flow is two dimensional. In each of these equations the drag force is a function of a number of different scalar quantities.

$$\frac{dV_x}{dt} = \frac{F_{Dx}(r, V_x, V_y, x, y)}{m(d)}$$
$$\frac{dV_y}{dt} = \frac{F_{Dy}(r, V_x, V_y, x, y)}{m(d)} \qquad 5.15$$
$$\frac{dx}{dt} = V_x$$
$$\frac{dy}{dt} = V_y$$

Where, d = diameter of the particle

x = x position

y = y position

V_x = x velocity of the particle

V_y = y velocity of the particle

By solving each of the equations with a Runge-Kutta variable time step integrator, the particle path can be numerically solved. At each time step during the integration, the fluid velocity field from the CFD solver is searched for the closest element to the particle's current position. Then the x and y velocity, as well as the temperature and kinetic energy at this fluid element are used to calculate the fluid turbulence intensity,

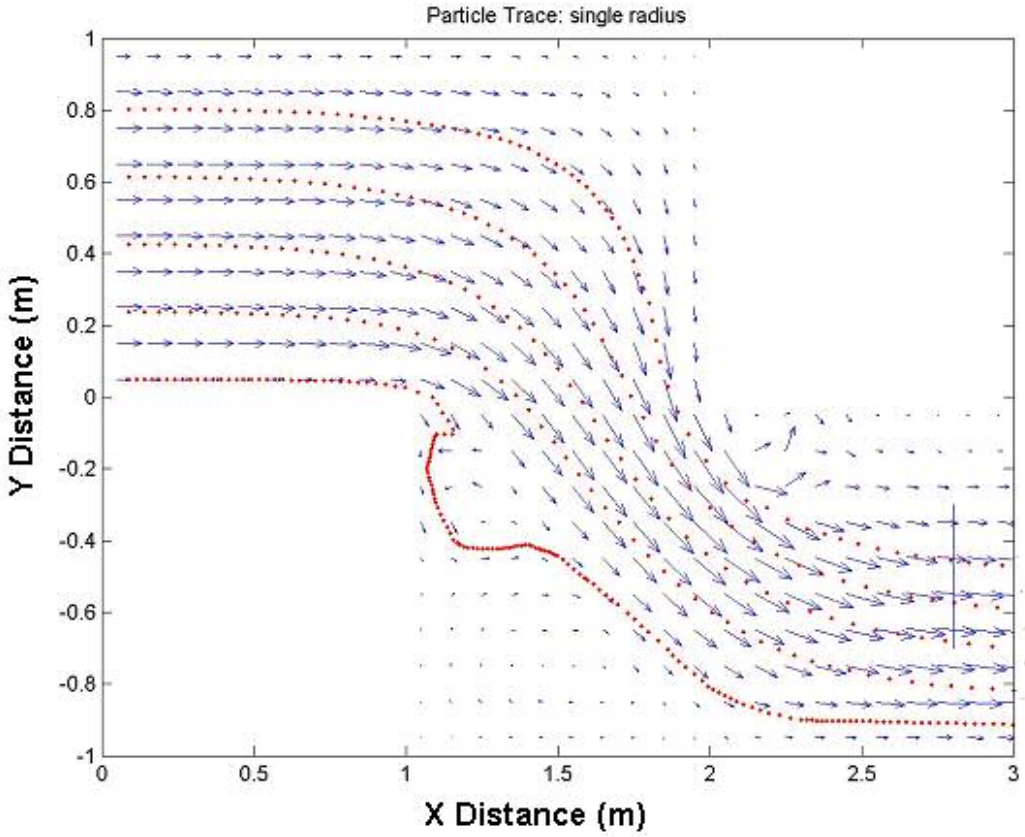

Figure 5.7 Particle Trajectory Calculated Using Lagrangian Integration, d= 1 micron

the drag force, and Brownian diffusivity for the particle at that moment. The code allows the particle paths to be calculated for any number of initial positions for varying particle diameters. The x and y positions as well as the particle Reynolds number are stored for every particle at each time step in a series of three dimensional matrices. This allows data manipulation after the computer has finished the numerical calculations.

Figure 5.7 shows the particle paths of several different sized particles through a test velocity field. It is evident that at diameters below one micron, the trajectories follow the streamlines, as the particle paths are nearly tangent to the velocity vectors. Figure 5.7 validates the use of the Stokes number calculation in section 5.5 to determine how well the particles follow the flow. This fact is used in future numerical models to

allow the Runge-Kutta integrator to be eliminated, thus decreasing computational time considerably.

5.7 Monte Carlo Model

The numerical model was subsequently refined to add the effects of fluctuating turbulent velocities and Brownian motion. Because the temperature and kinetic energy are known at each particle position, the Brownian diffusivity constant can be calculated using Equation 5.5. This diffusivity can be used to calculate a root mean square diffusion velocity for each particle via Equation 5.8. A Gaussian distributed random variable with standard deviation equal to the RMS velocity is calculated and added to the relative velocity of the particle. In effect the Brownian motion is added to the drag calculation by adjusting the relative velocity between the particle and the fluid over each time step.

To add the effects of fluctuating turbulent velocity to the model, another Gaussian random variable is used. At each time step the kinetic energy can be related to the turbulence intensity by:[4]

$$KE = I^2 \overline{U}^2 \qquad 5.16$$

Where, I = turbulence intensity

$\bar{U}$ = mean velocity of the flow

KE = kinetic energy of the flow

The turbulence intensity is defined as:

$$I = \frac{\sqrt{U'^2}}{\overline{U}} = \frac{U_{rms}}{\overline{U}} \qquad 5.17$$

Here, U_{rms} = the root mean square of the velocity in one direction.

Equations 5.16 and 5.17 can be combined to determine the standard deviation of the random turbulent velocity to be added to the relative velocity at each time step. Because the random turbulent motion creates particle paths with a unique trajectories, the best way to evaluate the particle movements is using a probability distribution plot. Using a Monte Carlo approach for each initial position and particle diameter, thousands of trajectories are calculated and stored in a four-dimensional array. Once the calculations are completed, the number of particles that have landed at any position can be divided by the total number of particles simulated to give a probability statistic. This method is often referred to as a Monte Carlo simulation because the model relies on random variables similar to rolling dice in a gambling casino.

5.8.1 Model Validation

To validate the Monte Carlo simulation of Brownian diffusion, a flow field of uniform velocity and zero turbulence intensity was created with the same dimensions as those in Figure 5.5. 3800 particles with diameters of 5, 10, and 100 nm were injected at a single point. The histogram plot of the number of particles at each radial distance downstream are shown in Figure 5.8. The histograms take on an obviously Gaussian distribution and the first standard deviation is marked on the plot. Notice that the value of one standard deviation is equal to the root mean square distance diffused shown in Figure 5.5. This confirms that using a random variable to model the Brownian motion

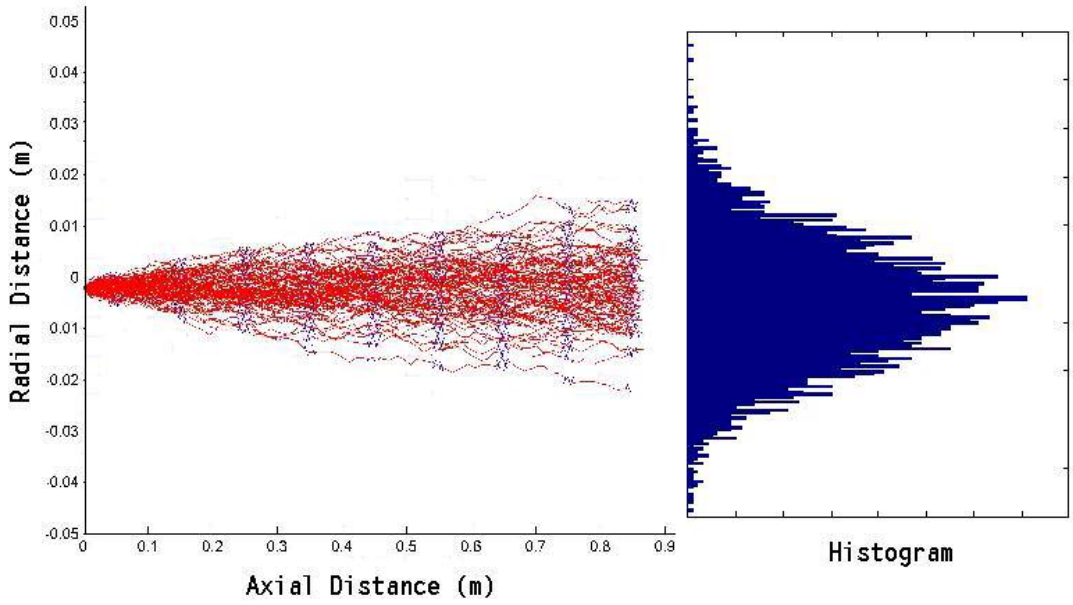

Figure 5.8 Particle Model Test, d = 10 nm

predicts particle behavior that exactly matches Einstein's equation. This validation suggests that this model can be used with more complicated velocity fields in the next section.

5.8 Model Results

By combining the methods from the previous sections, a model that predicts particle motion based on the fluid velocity field, turbulence intensity, and Brownian motion can be implemented. Figure 5.9 shows a plot of the vector field from Section 5.3 Fluent analysis, along with a number of simulated particle pathlines. In this case all of the particles have a diameter of 10 nanometers, and start at the same initial position. Obviously these small particles are affected the most by Brownian motion, which causes many of the particles to diffuse into the strong recirculation zone of the flow. Particles caught in this area of the flow exhibit a much longer residence time than particles

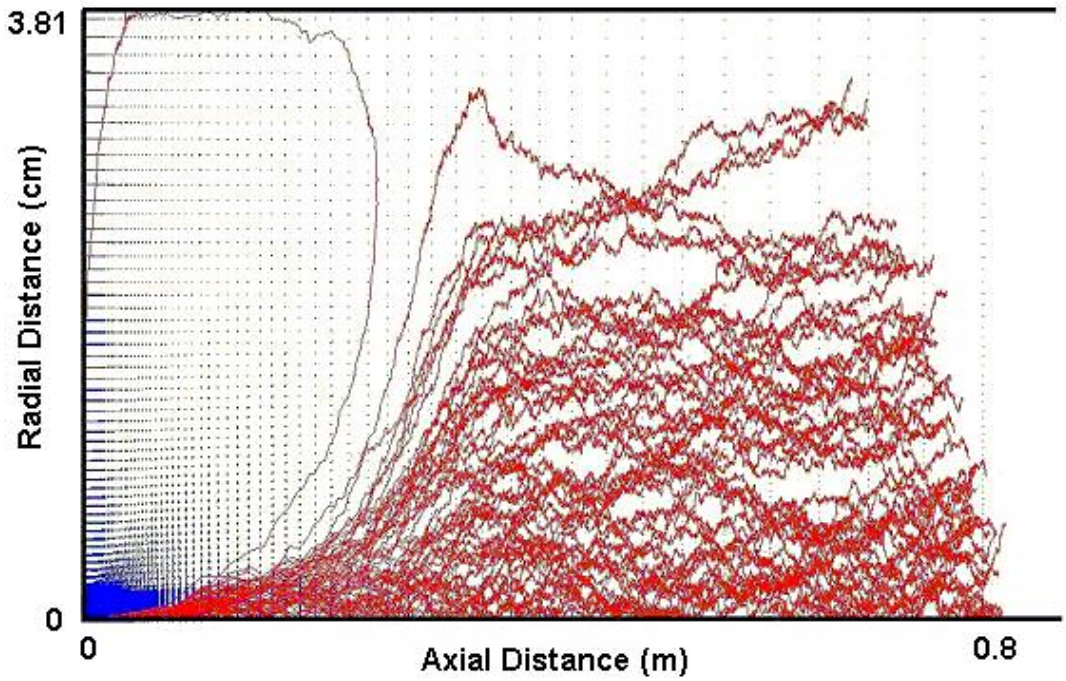

Figure 5.9 Particle Simulation, 100 Particles, D = 10 nm

following the axial jet. Figures 5.10 and 5.11 show similar plots with particles of 100 and 500 nm respectively. Because the larger particles are affected less by Brownian motion, they are less likely to reach the recirculation zone of the flow. A comparison of these three plots shows why dilution tunnel dynamics impact the size distribution so greatly. No matter where the sampling probe is inserted in the tunnel geometry, the measured particle size distribution will be heavily influenced by turbulence and the diameter-dependent diffusion.

Figure 5.12 shows the fraction of particles collected at several downstream locations using a 1/8 in diameter collection probe. Of interest is the fact that as axial distance increases, the fraction collected decreases, indicating a greater dilution ratio, as

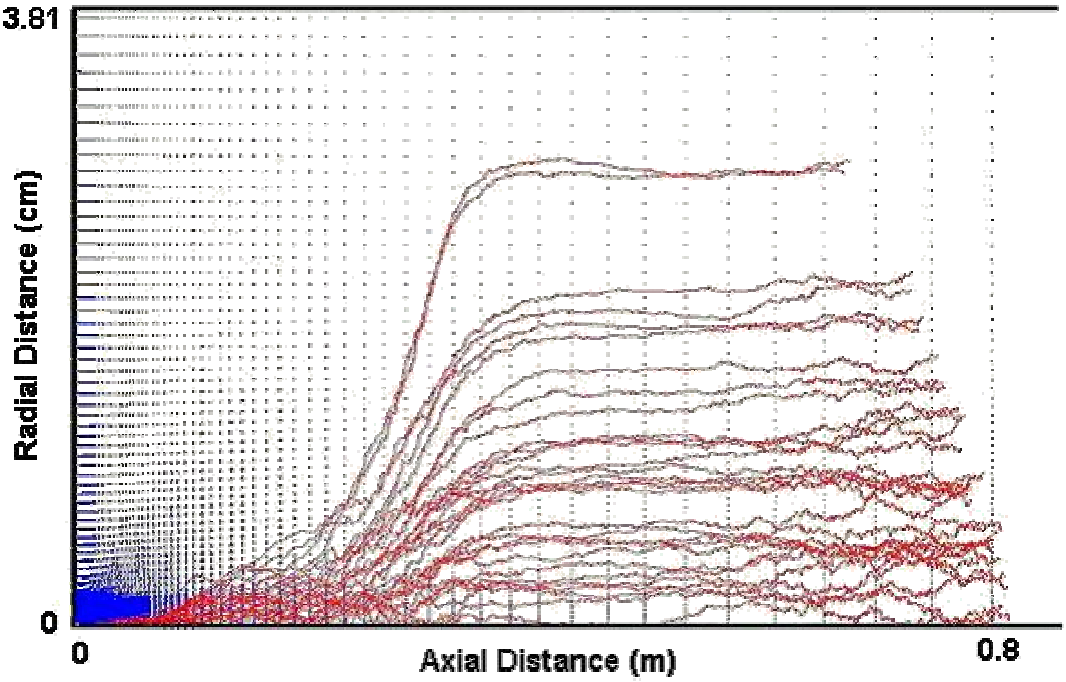

Figure 5.10 Particle Simulation, 30 Particles, D = 100 nm

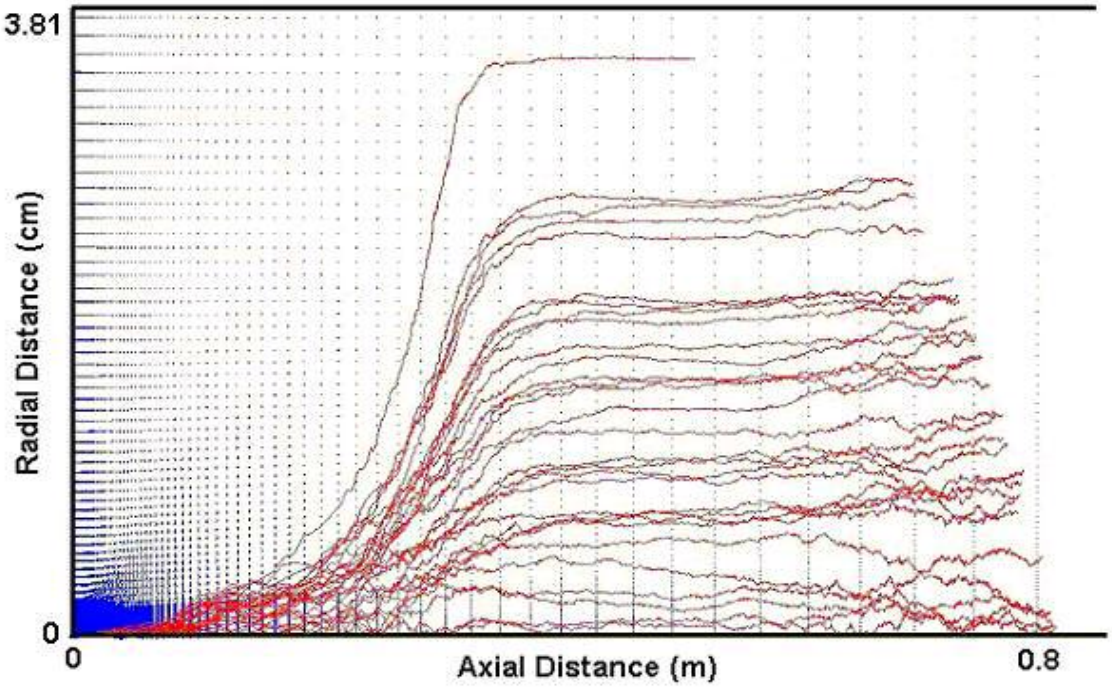

Figure 5.11 Particle Simulation, 30 Particles, D = 500 nm

was expected. If each of the three curves is normalized to bring them on top of each other, they are not similar. This shows that varying probe axial position influences not only the overall dilution ratio, but also the dilution ratio at specific particle diameters. The general trend seen in Figure 5.11 shows an increase in collection efficiency (at the centerline) at larger diameters, which is expected. An irregularity occurs in the model at a particle diameter of 10 nm. Here the capture fraction increases greatly, despite the fact that these smallest particles should diffuse the most, and hence have the largest dilution ratio. When the numerical results are compared with the capture fraction recorded by the SMPS as described in Section 4.7, this very high capture fraction is also observed in

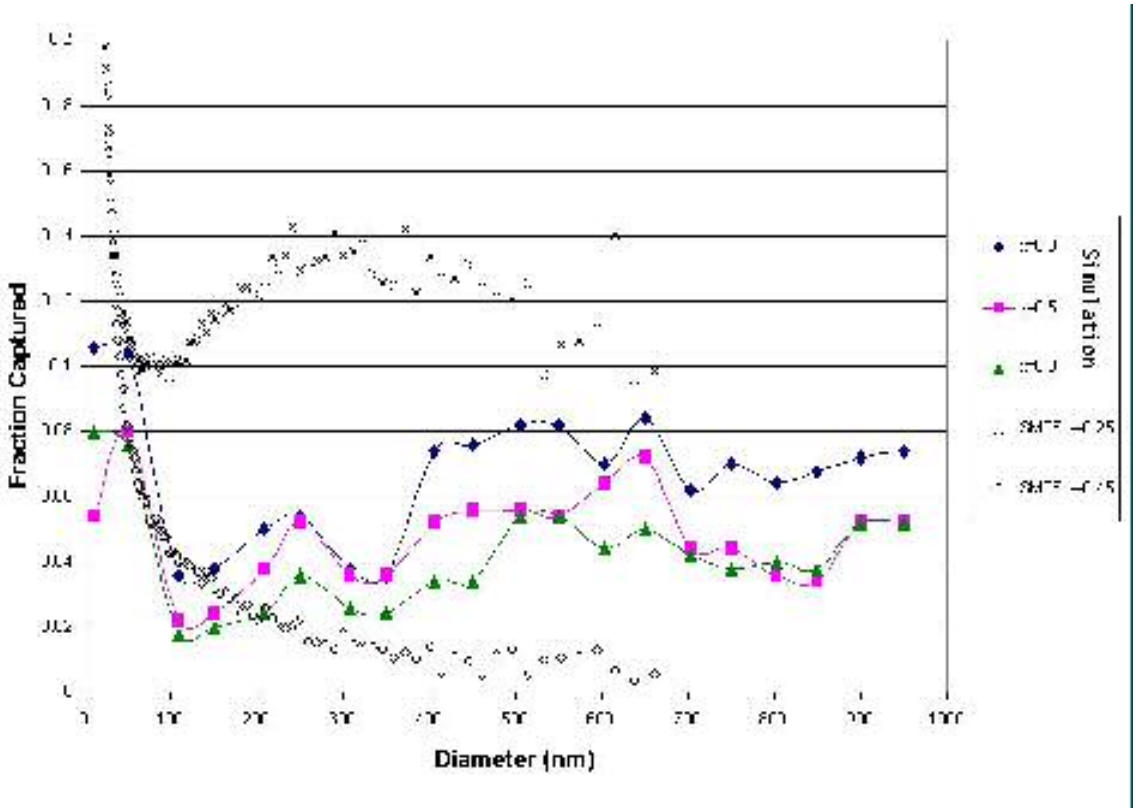

Figure 5.12 Simulated Particle Collection at Various Axial Positions with experimental SMPS data

experiments for diameters smaller than 50 nm. Further comparison between the SMPS results and the numerical simulation show only the magnitude of the fraction is similar

and any trends seen in the simulation cannot be duplicated with the experimental results. One possible cause of these discrepancies between experimental data and numerical model is the turbulence modeling method. The model uses the K term from the CFD solution to determine the turbulence intensity and thus fluctuating velocity. This in no way captures any information about eddy structures which most certainly affect the particle dynamics.

CHAPTER 6 Conclusions

6.1 Summary

The fluid dynamics and particulate behavior inside a miniature dilution tunnel were studied with a variety of methods. Several separate experimental methods yielded similar information about the velocity field, which was consistent with preexisting literature on the subject of confined jets. The velocity data recorded using the LDV setup closely followed the expected jet behavior. A more reliable particle seeding method would have made the LDV results more repeatable. The NOx experiment allowed actual residence times to be measured, and yielded some important information about the turbulent structure of the flow. Velocity data calculated from this experiment, while crude, conformed to the expected rate of jet decay. The flow visualization experiments, yielded the most directly useful results. From the frame by frame pictures velocity and eddy size estimates could be obtained and compared with other results. More importantly the visualization highlighted the presence of strong recirculation zones. All of the aforementioned experiments verify the complex fluid behavior inside the dilution tunnel, which complicates aerosol transport.

For a comparison to the previous experimental results, both analytical and numerical modeling was performed on the fluid dynamics of the tunnel. The jet decay was determined based of the analytical solution to a free turbulent jet, and compared to experimental results from several journal articles.[12,14,15,19] The results from a K-ε closure numerical model were then compared with both the analytical solution and experimental results. The CFD results showed good agreement with the results in

Chapter 4, which helps to justify the use of the velocity field from the CFD in the Monte Carlo model. Using a Reynolds averaging numerical method to solve the fluid dynamics calculates only the mean values of velocity. This unfortunately hides any effects of eddy mixing that is present in the actual flow.

Knowledge of the fluid field is only half of the equation for predicting the aerosol behavior. The effects of Brownian motion heavily influence the dilution process, and more importantly, influence different sized particles to different degrees. If insufficient residence times are present in the tunnel, Brownian motion can bias a particle size distribution based upon particle diameter. To determine how Brownian motion, and turbulent energy might affect the output size distribution, a numerical model was developed. Using a velocity field given by a CFD solver, the model calculated the particle trajectories and used a Monte-Carlo type method to determine the concentration at the tunnel output. Results from this model confirmed that particle size distributions varied greatly based on output probe position.

6.2 Contributions of this Research

The results of this thesis lend insight into future designs of miniature dilution tunnels. To eliminate the entrainment of particles into recirculation zones, a jet type input to the dilution tunnel should be avoided. Instead, the dilution air should flow through a constant diameter pipe, while the exhaust is fed into the center of the tunnel. This would eliminate the step flow that creates the recirculation zones and allow the sample to follow a more predictable path. Eliminating the complex fluid dynamics will not guarantee an unbiased dilution tunnel. The tunnel must be designed to negate the

effects of particle diffusion upon the output size distribution. To achieve this, the tunnel must be made sufficiently long, or mixing must be enhanced through fluid motion.[7,17] In both cases, a particle dynamic model such as the one developed in Chapter 5 will allow designs to be validated.

6.3 Future Work

If the current dilution tunnel design were to continue in use, further study would be necessary to correct for a bias caused by the tunnel configuration. The flow visualization experiment yielded the most insight into the fluid dynamics and could be improved upon. Substituting a laser sheet for the 3D light source used would allow much crisper images to be taken. By pulsing this laser and using PIV software, accurate velocity measurements could be made, showing not just mean velocities but also turbulent eddy structures. Because the velocity field given by the CFD code is somewhat suspect due to necessary simplifications in the solution, the information gained through PIV could enhance the results from the Monte Carlo model significantly.

To evaluate the accuracy of the Monte Carlo model, further experiments using known aerosol sources and an SMPS are needed. Through investigation of the measured particle size distribution at different probe conditions and flowrates, a comparison between the actual dynamics of the tunnel, and the Monte Carlo method could be achieved.

BIBLIOGRAPHY

[1] Abramovich, G.N. *Theory of Turbulent Jets.* MIT Press. (1963).

[2] Bagley, S., et al. "Characterization of Fuel and Aftertreatment Device Effects on Diesel Emissions." *Health Effects Institute Research report No 76.* (1996).

[3] Baron, P.A. and Willeke, K., ed. *Aerosol Measurement.* Wiley-Interscience. (2001).

[4] Bernard, P.S., Wallace, J.M. *Turbulent Flow, Analysis Measurement and Prediction.* John Wiley and Sons. Hoboken, NJ (2002).

[5] Friedlander, S.K. *Smoke Dust and Haze.* Oxford University Press. (2000).

[6] Katragadda, S., Bata, R. and McCawley, M. "Calculations of Flow and Mixing Properties in a Two-Dimensional Dilution Tunnel." *Intl Journal of Computer Applications in Tech.* Vol 11, No 3/4/5. (1998).

[7] Kayes, D. and Hochgreb, S. "Investigation of the Dilution Process for Measurements of Particulate Matter from Spark-Ignition Engines." *SAE 982601*. (1998).

[8] Kittleson, D.B., et al. "Characterization of Diesel Particles in the Atmosphere." *CRC, AP-2 Project Group*. (1988).

[9] Kittleson, D.B., et al. "Diesel Aerosol Sampling in the Atmosphere" *SAE 2000-01-2212.* (2000).

[10] Munson, B.R., Young, D.F. and Okiishi, T.H. *Fundementals of Fluid Mechanics.* John Wiley and Sons. New York. (1998).

[11] Panton, R.L. *Incompressible Flow.* John Wiley and Sons. New York. (1996).

[12] Park, C.J. and Chen, L.D. "Experimental Investigation of Confined Turbulent Jets." *AIAA Journal.* Vol 27. No 11. (1989).

[13] Pope, S.B. *Turbulent Flows*. Cambridge University Press. (2000).

[14] Risso, F. and Fabre, J. "Diffusive Turbulence in a Confined Jet Experiment." *Journal of Fluid Mechanics.* Vol 337. pp 233-261. (1997).

[15] Teyssandier, R.G. and Wilson, M.P. "An Analysis of Flow Through Sudden Enlargements in Pipes." *Journal of Fluid Mechanics.* Vol 64. pp 85-95. (1974).

[16] TSI Inc. *Model 3936 SMPS (Scanning Mobility Particle Sizer) Instruction Manual.* Febuary (2001).

[17] Wei, Q., Kittelson, D.B., Watts, W.F. "Single Stage Dilution Tunnel Design" *SAE 2007-01-0207.* (2001).

[18] Wei, Q., Kittelson, D.B., Watts, W.F. "Single Stage Dilution Tunnel Performance" *SAE 2001-01-0201.* (2001).

[19] Yang, B.T. and Yu, M.H. "The Flowfield in a Suddenly Enlarged Combustion Chamber." *AIAA Journal.* Vol 21. No 1. (1983).

APPENDIX A: Auxiliary Diagrams

Dilution Tunnel Side View

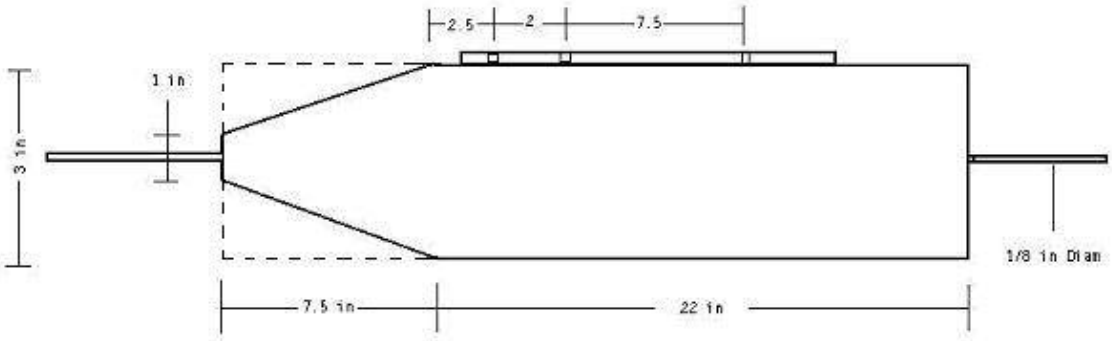

Dilution Tunnel Top View

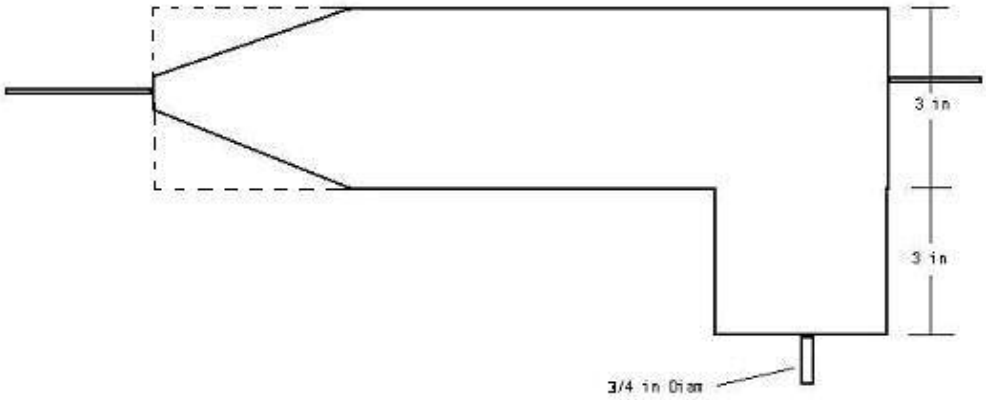

9 Thermocouple Probe

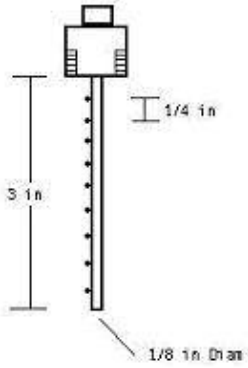

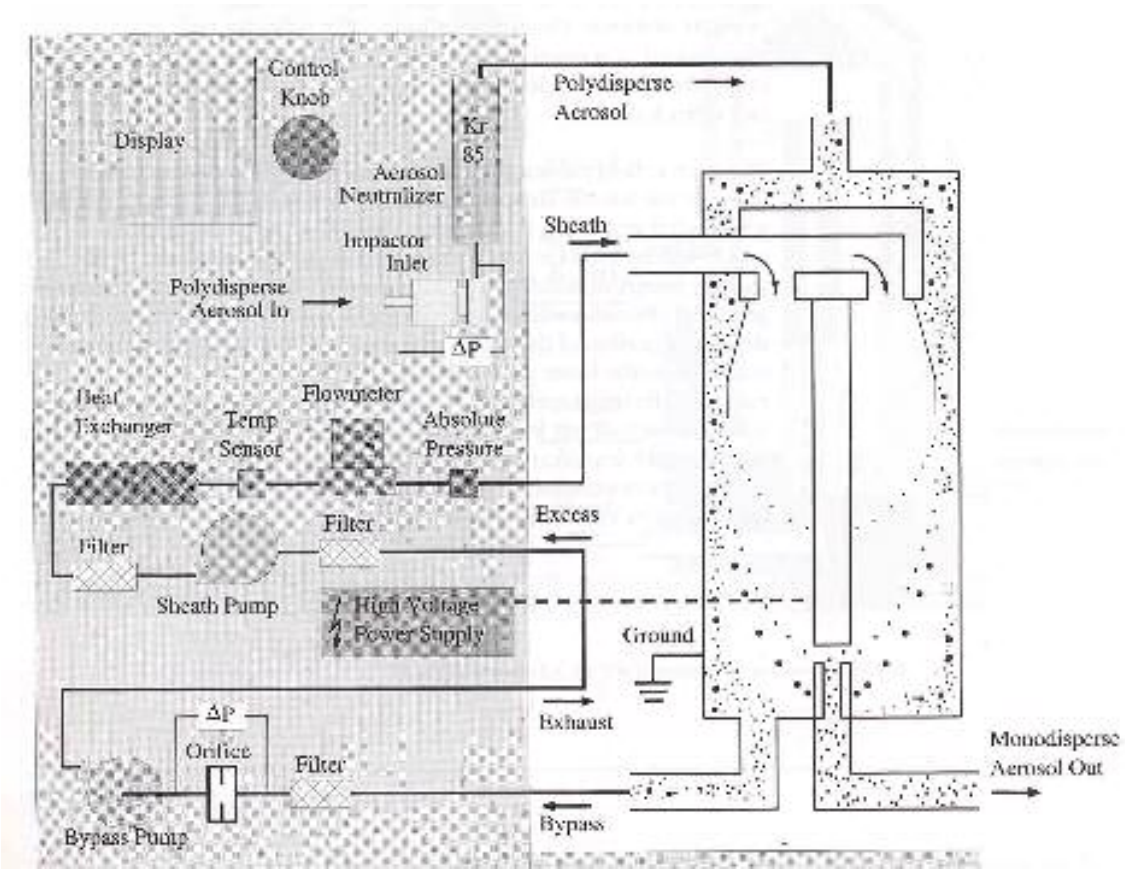

SMPS Internal Schematic [16]